Journal of Nuclear Medicine, published on December 5, 2019 as doi:10.2967/jnumed.119.231068

Differential expression of glucose transporters and hexokinases in prostate cancer with a neuroendocrine gene signature: a mechanistic perspective for FDG imaging of PSMA-suppressed tumors

Martin K. Bakht[1,2,3], Jessica M. Lovnicki[4], Janice Tubman[1], Keith F. Stringer[1,5], Jonathan Chiaramonte[6], Michael R. Reynolds[6], Iulian Derecichei[1], Rosa-Maria Ferraiuolo[7], Bre-Anne Fifield[1], Dorota Lubanska[1], So Won Oh[2,3], Gi Jeong Cheon[2,3*], Cheol Kwak[8], Chang Wook Jeong[8], Keon Wook Kang[2,3], John F. Trant[6], Colm Morrissey[9], Ilsa M. Coleman[10], Yuzhuo Wang[4], Hojjat Ahmadzadehfar[11], Xuesen Dong[4], Lisa A. Porter[1*]

[1]*Department of Biomedical Sciences, University of Windsor, Windsor, Ontario, Canada*

[2]*Department of Nuclear Medicine, Seoul National University College of Medicine, Seoul, Korea*

[3]*Laboratory of Molecular Imaging and Therapy, Cancer Research Institute, Seoul National University College of Medicine, Seoul, Korea*

[4]*Vancouver Prostate Centre, Department of Urologic Sciences, University of British Columbia, Vancouver, BC, Canada*

[5]*Department of Pathology, Cincinnati Children's Hospital Medical Center, Cincinnati, Ohio, USA*

[6]*Department of Chemistry and Biochemistry, University of Windsor, Windsor, Ontario, Canada*

[7]*Barbara Ann Karmanos Cancer Institute, Detroit, Michigan, USA.*

[8]*Department of Urology, Seoul National University College of Medicine, Seoul, Korea*

[9]*Department of Urology, University of Washington, Seattle, Washington, USA*

[10]*Divison of Human Biology, Fred Hutchinson Cancer Research Center, Seattle, Washington, USA*

[11]*Department of Nuclear Medicine, University Hospital Bonn, Bonn, 53127, Germany*

Word count: 4998

Running title: Glucose transport in neuroendocrine PC

Co-corresponding authors*:

***Gi Jeong Cheon,** *MD PhD*

Department of Nuclear Medicine, Seoul National University College of Medicine, Seoul 110-744, Korea

larrycheon@snu.ac.kr

***Lisa A. Porter,** *PhD*

Department of Biomedical Sciences, University of Windsor, Windsor, Ontario, N9B 3P4, Canada

lporter@uwindsor.ca

First author:

Martin K. Bakht, *PhD candidate*

Department of Biomedical Sciences, University of Windsor, Windsor, Ontario, Canada.

khosra11@uwindsor.ca

Financial support: This study was supported by Canadian Institutes of Health Research (#142189 (LAP) & #PJT156150 (XD)), Natural Sciences and Engineering Research Council of Canada #2018-06338 (JFT) and a grant of the Korea Health Technology R&D Project through the Korea Health Industry Development Institute (KHIDI), funded by the Ministry of Health & Welfare, Republic of Korea (#H18C1916 (GJC&KWK). The financial support of TELUS Ride for Dad, Prostate Cancer Fight Foundation (LAP) and Ontario Trillium Scholarship Program (MKB) is greatly appreciated. The gene expression analysis was supported in part by a Department of Defense Idea Development Award-Partnering-PI (W81XWH-17-1-0414;W81XWH-17-1-0415 (CM)) and the Pacific Northwest Prostate Cancer SPORE (P50CA97186 (CM)).

ABSTRACT

Purpose Although the incidence of *de novo* neuroendocrine prostate cancer (NEPC) is rare, recent data suggests that low expression of prostate-specific membrane antigen (PSMA) is associated with a spectrum of neuroendocrine (NE) hallmarks and androgen receptor (AR)-suppression in prostate cancer (PC). Previous clinical reports indicate that PCs with a phenotype similar to NE tumors can be more amenable to imaging by ^{18}F-Fluorodeoxyglucose (FDG) rather than PSMA-targeting radioligands. In this study, we evaluated the association between NE gene signature and FDG uptake-associated genes including glucose transporters (GLUTs) and hexokinases, with the goal of providing a genomic signature to explain the reported FDG-avidity of PSMA-suppressed tumors.

Methods Data mining approaches, cell lines and patient-derived xenograft (PDX) models were used to study the levels of 14 members of the *SLC2A* family (encoding GLUT proteins), 4 members of the hexokinase family (genes: *HK1* to *3* and *GCK*) and PSMA (*FOLH1* gene) following AR-inhibition and in correlation with NE hallmarks. Also, we characterize a NE-like PC (NELPC) subset among a cohort of primary and metastatic PC samples with no NE histopathology. We measured glucose uptake in a NE-induced *in vitro* model and a zebrafish model by non-radioactive imaging of glucose uptake using fluorescent glucose bioprobe, GB2-Cy3.

Results This work demonstrates that a NE gene signature associates with differential expression of genes encoding GLUT and hexokinase proteins. In NELPC, elevated expression of *GCK* (encoding glucokinase protein) and decreased expression of *SLC2A12* correlated with earlier biochemical recurrence. In tumors treated with AR-inhibitors, high expression of *GCK* and low expression of *SLC2A12* correlated with NE histopathology and PSMA gene suppression.

GLUT12-suppression and amplification of glucokinase was observed in NE-induced PC cell lines and PDX models. A higher glucose uptake was confirmed in low-PSMA tumors using a GB2-Cy3 probe in a zebrafish model.

Conclusions NE gene signature in NEPC and NELPC associates with a distinct transcriptional profile of GLUTs and HKs. PSMA-suppression correlates with GLUT12-suppression and glucokinase-amplification. Alteration of FDG uptake-associated genes correlated positively with higher glucose uptake in AR and PSMA-suppressed tumors. Zebrafish xenograft tumor models are an accurate and efficient pre-clinical method for monitoring non-radioactive glucose uptake.

Key words: Neuroendocrine prostate cancer, PSMA, glucose transporters, hexokinases, glucokinase

INTRODUCTION

The androgen receptor (AR) plays a central role in regulating the transcriptional events driving prostate cancer (PC) progression and development of metastatic castration-resistant prostate cancer (mCRPC) (*1*). AR-inhibition is an effective therapeutic approach for most patients at different stages of PC. Although the incidence of *de novo* neuroendocrine (NE) PC (NEPC) is considered rare, several emerging forms of PC with low-levels of AR are identified. The suppression and low activity of AR in these patients is largely associated with a NE gene signature (NEGS) and resistance to AR-inhibition (*2,3*).

AR-directed therapy of mCRPC could promote cellular plasticity and development of an AR-suppressed phenotype similar to NEPC which manifests the histopathology of NE disease (*4*). Another emerging phenotype of mCRPC is AR-null and NE-null, classified as double-negative PC (DNPC) (*3*). A recent molecular subtyping of PC patients with no history of AR-directed therapies identified a NE-positive subtype with low chromatin binding and activity of AR. These patients have been referred to as NE-like PC (NELPC) since they do not represent the NE-histopathology (*2,5*). NEPC is associated with the loss of RE1-silencing transcription factor (REST) due to alternate splicing by the RNA splicing factor serine/arginine repetitive matrix 4 (*SRRM4*). *SRRM4* plays a crucial role in progression to NEPC under next-generation AR-inhibitors, such as abiraterone and enzalutamide (*6*). Hence, the elevation of *SRRM4* and the loss of its target *REST* could be specific markers of treatment-induced NEPC.

AR regulates the expression of *FOLH1* gene encoding the transmembrane protein, prostate-specific membrane antigen (PSMA). PSMA-targeted molecular imaging and therapy are transforming the landscape of PC management (*7,8*). Despite the impactful implications of PSMA, there are clinical reports that suggest that PSMA-targeted imaging does not effectively visualize

NEPC tumors (*8-10*). Pre-clinical studies confirmed that the induction of lineage plasticity by AR-inhibition leads to NE-transdifferention and suppression of PSMA (*11*).

Similar to glucose, ^{18}F-fluorodeoxyglucose (FDG) is actively transported into the cell by the protein family of glucose transporters (GLUTs), encoded by *SLC2A* genes, followed by phosphorylation by hexokinase (*12*). In some types of tumors a positive correlation has been reported between FDG uptake and the levels of specific GLUTs and hexokinases (*12-14*). FDG-positron emission tomography (PET) is a well-accepted approach for delineation of proliferative and poorly-differentiated/dedifferentiated NE-tumors (*15*). Despite this, FDG-PET has been considered ineffective in assessing metastatic tumor burden and monitoring therapy response (*16*). Recent case reports illustrate NEPC delineation may be more feasible by FDG than PSMA-radioligands (*17,18*) and Spratt *et al*. (*19*) demonstrated the utility of FDG-PET for NEPC imaging. Interestingly, Thang *et al.* (*20*) screened patients with ^{68}Ga-PSMA-11 and FDG-PET and they identified a subset of patients with low PSMA-radioligand uptake and high FDG uptake.

Development of non-radioactive glucose analogs enabling the delineation of the glucose uptake of tumors have been studied using a variety of optical approaches mostly in mouse models (*21*). PC xenograft studies in zebrafish are coming to the forefront as a cost-effective and time-efficient model for drug screening, and the fluorescent glucose bioprobe GB2-Cy3 has been used to monitor glucose uptake in a zebrafish model (*22,23*). However, the feasibility of monitoring of glucose uptake in PC in a zebrafish model has not been evaluated.

In this work we used data mining approaches, cell lines and patient-derived xenograft (PDX) models to study expression levels of glucose uptake-associated genes including GLUTs and hexokinases in NEPC and NELPC to provide a genomic rationalization for the previously reported

FDG-avidity of PSMA-suppressed PC tumors. We also present the feasibility of non-radioactive *in vivo* imaging of glucose uptake using a zebrafish model.

MATERIAL AND METHODS

Cell Culture

The LNCaP cell line was purchased from ATCC and grown in RPMI-1640 in the presence of 10% fetal bovine serum. Progression to NEPC was achieved by culturing LNCaP cells in RPMI1640 medium with 10% charcoal-stripped serum for 4 months. Under these conditions, cell morphology gradually changed into a mixture of a NE-like phenotype and a non-NE-phenotype. After 4 months, a subclone with a NE-like phenotype was isolated (LNCaP-NEPC). LNCaP cells, maintained in RPMI-1640 + fetal bovine serum, were used as a control and are referred to as LNCaP-AdPC.

Antibodies

The immunoblotting technique used was previously described (*11*). Antibodies are as follows: actin (Chemicon-Millipoure; MAB150-1R), PSMA (Cell Signaling; D4S1F), AR (Santa Cruz Biotechnology (SCB); sc-816), NSE (SCB; sc-271384) and GCK (SCB; sc-17819) and GLUT12 (Abcam; ab100993).

Data Mining Analysis

Using 268 PC samples from 3 different cohorts we assessed the transcript abundance for all of the *SLC2A* family (*SLC2A1-14*) and the HK family (*HK1-4, HK4* referred to as *GCK*). In addition, we monitored the PSMA gene (*FOLH1*), the NE-marker synaptophysin gene (*SYP*), *SRRM4* as a positive-marker of treatment-induced NEPC and *REST* as negative-marker of NEPC. Patients with lack of NEGS or NE histopathology are referred as adenocarcinoma PC (AdPC).

To assess the lineage plasticity of mCRPC, samples from a tissue acquisition necropsy platform established at the University of Washington (UW) were used (*3*). All rapid autopsy tissues were collected from patients who signed written informed consent under the aegis of the Prostate Cancer Donor Program at the UW and the Institutional Review Board of the UW approved this study. We classified our mCRPC subtypes as AdPC (AR^{+}/NE^{-}), AR-suppressed AdPC (AR^{low}/NE^{-}), NEPC (AR^{-}/NE^{+}), and DNPC (AR^{-}/NE^{-}). In addition, we used the Beltran cohort (*4*) with histologically confirmed mCRPC-AdPC and mCRPC-NEPC samples. We identify a NELPC subset among AdPC tumors from the Memorial Sloan Kettering Cancer Center (MSKCC) cohort (*24*) using the meta-signature of prototypical high-grade NEPC (*25*). Gene set enrichment analysis was performed on the identified subsets using gene sets downloaded from the Molecular Signatures Database (*26*).

Mice PDX Models

Fresh PC tissues from patients were grafted under the kidney capsules of non-obese diabetic/severe combined immunodeficient mice. Institutional Review Board and Animal Care Committee of the University of British Columbia approved this study and all subjects signed a written informed consent. We previously characterized and validated these models (*27*).

GB2-Cy3 Synthesis and Cellular Uptake

Synthesis and *in vitro* uptake of a glucose bioprobe GB2-Cy3 was previously reported with some modifications (*22,28,29*). Full experimental details are provided in the Supplemental Material and Supplemental Schemes 1-2 summarize GB2-Cy3 synthetic strategy.

***In Vivo* Glucose Uptake Imaging**

Wild-type zebrafish (*Danio rerio*) were maintained following the Canadian Council on Animal Care Guidelines. *In vivo* uptake of GB2-Cy3 in was visualized in a zebrafish model by

modifications of previous protocols (*23,30*). Full experimental details are provided in the Supplemental Material. This study was approved by the University of Windsor Animal Care Committee.

Statistical Analysis

Statistical analysis was done using GraphPad Prism (CA, USA). The results are expressed as the mean ± standard error of the mean (SEM). The box-whisker plots show the median (horizontal line), the interquartile range (margins of box) and the absolute range (vertical line). Differences between two groups were compared by unpaired Student's t-test. One-way ANOVA followed by a Benjamini-Hochberg or Tukey adjustment. Neurite length was measured by manual tracing and determined using NIH ImageJ software as previously described (*11,31*). Pearson correlation was used for nearest neighbor analysis and pairwise-correlation of the studied genes. Kaplan-Meier plots and heatmaps were generated using camcAPP (*32*) and Broad Institute Morpheus software (MA, USA).

RESULTS

Differential Expression of *FOLH1*, *SLC2A* and *HK* in mCRPC

Figure 1A shows that expression of *SLC2A12* and *FOLH1* are the nearest neighbors to *AR* ($r > 0.6$, $P < 0.01$) and *GCK* is the furthest neighbour ($r = -0.6$, $P < 0.01$) in the UW cohort (*3*). We observed a significant suppression of *FOLH1* in low-AR mCRPC phenotypes including NEPC and DNPC samples (Fig. 1B). Figure 1C shows NEPC tumors have a 5-fold elevation of *GCK* ($P < 0.0001$) when compared to AR-positive samples. Alternatively, Fig. 1D demonstrates that NEPC and DNPC samples suppress expression of *SLC2A12*. Supplemental Figure 1 verifies that in the Beltran cohort (*4*) *FOLH1*-suppressed NEPC samples have similar profiles of glucose transporter

gene expression. In summary, *GCK* gene expression is elevated and the *SLC2A12* gene is suppressed in NEPC.

Differential Expression of *SLC2A* and HK in NELPC

The meta-signature of prototypical high-grade NEPC (*25*) was employed to isolate a potential NELPC group among a population of metastatic and primary AdPC samples lacking NEPC histopathology (Supplemental Figs. 2 and 3). Figure 2A shows the transcriptionally identified NELPC subset have shorter time to biochemical recurrence in NELPC (log-rank *P*-value = 0.02). Figure 2B displays that a NELPC hallmark can be observed in both primary and metastatic samples, with the more prevalent signature seen in metastatic and high Gleason score samples. Figure 2C shows a lack of hallmarks of AR response in NELPC. Supplemental Figure 4 shows that *SLC2A1, 3-5, 9, 10, 12-14* and *HK1, 2* genes cluster with *REST*; herein referred to as *REST*-clustered genes. On the other hand, *SLC2A2, 6-8, 11, HK3* and *CGK* cluster with *SRRM4* and other NE-markers; herein referred to as *SRRM4*-clustered genes. Pairwise-correlation with *SRRM4* expression is presented in Supplemental Figures 5-7. Similar to NEPC, *SLC2A12* and *FOLH1* expression are decreased in NELPC relative to AdPC (Fig. 2D). *GCK* expression is significantly higher in NELPC.

The Association of *SLC2A* and *HK* with Gleason Score and Biochemical Recurrence in NELPC

Supplemental Figures 8-10 depict expression levels of the studied genes during progression of AdPC based on Gleason score. The majority of *REST*-clustered *SLC2A* genes and *HKs* are either unchanged or suppressed at high Gleason scores while *SRRM4*-clustered genes are significantly increased in samples with high Gleason scores. Kaplan-Meier survival curves studying high and low expression levels of the studied genes are represented in Supplemental Figures 11-13. The

high expression of *SRRM4*-clustered genes such as *GCK* and *REST*-clustered gene *SLC2A1* (as an exception) are significantly associated with decreased biochemical recurrence (log-rank *P*-value for *GCK*: 0.015). Interestingly, high levels of *REST*-clustered genes including *SLC2A12* are associated with shorter time to biochemical recurrence (log-rank *P*-value for *SLC2A12*: 0.012). Supplemental Table 1 summarises the performed analysis on NELPC.

SLC2A12 Suppression and _GCK_ Overexpression are Shared Among NEPC and NELPC

RNA-seq data from 268 PC samples from the MSKCC (*24*), Beltran (*4*) and UW (*3*) cohorts were used to stratify *SLC2A1-14* and *HK1-4* genes into NE-clustered and AdPC-clustered groups (Supplemental Fig. 14). The intersection between the clustered genes in different cohorts and inclusion of the most differentially expressed genes showed that *GCK* is the most highly expressed gene and *SLC2A12* is the most suppressed gene in samples with a NEGS.

NEPC Has a Distinct _GCK_-Amplified and _SLC2A12_-Suppressed Signature in PDX Models

The LTL331 PDX is a model of PC progression from AdPC-to-NEPC. LTL331 tumors regress following castration, but relapse within 24 to 32 months with tumors harbouring NEPC phenotypes (*27*). Figure 3A demonstrates that *GCK* expression is minimal before progression to CRPC but reaches maximum levels following cellular plasticity to CRPC and NEPC. Conversely, *SLC2A12* expression is at its maximum level in hormone sensitive AdPC and, with a slight fluctuation, gradually levels decrease following castration. The expression of *SLC2A12* and *FOLH1* are the nearest neighbors to *AR* ($r > 0.6$, $P < 0.01$) and *GCK* is the furthest neighbour ($r = -0.87$, $P < 0.01$) in the UW cohort (*3*). Figure 3B shows in our other well characterized PDX models consisting of 20 AdPC and 3 NEPC models that we observe significant elevation of *GCK* and suppression of *SLC2A12* gene expression in the NEPC models. Overall, NEPC models have a *SLC2A12*-low and *GCK*-high signature.

Higher *In Vitro* and *In Vivo* Glucose Uptake in NE-induced Cell Lines

To investigate the role of progression to a NE phenotype on glucose uptake we used the well-characterized NE subclone cell line (LNCaP-NEPC) in which NEPC cells are derived from LNCaP cells (LNCaP-AdPC) by culturing in an androgen-depleted environment to mimic clinical androgen-deprivation therapy (*33*) (cartoon of process: Supplemental Fig. 15A; characterization of lines in Supplemental Fig. 15B-D). Figure 4A shows that protein levels of the NE-marker NSE are increased in the LNCaP-NEPC, while PSMA and AR levels are significantly decreased. The LNCaP-NEPC cell line has a significantly higher level of glucokinase (GCK) protein and a significantly lower level of GLUT12 (Fig. 4B).

Supplemental Figures 16-23 demonstrate chemical characterisation of the GB2-Cy3. Supplemental Figure 24 illustrates GB2-Cy3 uptake and its localization in LNCaP cells. Figure 4C shows the LNCaP-NEPC cell line has a higher *in vitro* uptake of GB2-Cy3. Similarly, a zebrafish model was used for non-radioactive *in vivo* imaging of glucose uptake and displayed higher GB2-Cy3 in engrafted LNCaP-NEPC cells (Fig. 5). These observations indicate that suppression of PSMA, AR and elevation of NE-markers in LNCaP cell lines are associated with a differential level of glucose uptake, suppression of GLUT12 and elevation of glucokinase proteins.

DISCUSSION

The development of AR-indifferent and NE-positive tumor phenotypes through divergent clonal evolution as a mechanism of resistance to AR-inhibition in mCRPC is a well characterized concept (*3,4*). However, Stelloo *et al.* (*2*) identified a NELPC in a treatment naïve and primary cohort. Our work identified a NELPC subset among primary and metastatic samples with no history of exposure to next generation AR-inhibitors. Our data also shows that the incidence of NELPC is more prevalent in metastatic specimens. These data support that either AR-indifferent

subsets of cells can exist among AdPC that possess a greater susceptibility for NE-transdifferentiation, or AR-indifferent, NE-like cells exist from an early time point and are gradually selected for during treatment pressures.

Clinically there is data to support the detection rate of ^{68}Ga-PSMA-11 correlates with the prostate-specific antigen level (*7*). Also, patients with low levels of prostate-specific antigen show lower PSMA-radioligand uptake and higher FDG uptake (*18,20*). This supports the goals of this study to investigate the mechanistic basis for FDG-avidity in NEPC and DNPC. Here we show that the isoforms of GLUTs are structurally and functionally related proteins with different affinities to glucose. They are expressed in different cells based on the metabolic necessity for glucose uptake (*34*). The elevation of glycolysis in NEPC has been previously reported (*35,36*). Irrespective of overall contribution of GLUT in glucose metabolism, GLUT and HK family members could be associated with FDG uptake (*13,14*). Like glucose, FDG is phosphorylated by HKs while their products, glucose-6-phosphate and FDG-6-phosphate, could have different levels of inhibition on HKs depending on their structure (*37*). Supplemental Figure 25 represents structural domains of the isoforms of human HK proteins (*38*). Glucokinase lacks the N-terminus domain and cannot be inhibited by either glucose-6-phosphate or FDG-6-phosphate.

GLUT11 is considered a high affinity glucose transporter and could be effectual in elevation of glucose uptake while it is amplified (*34*). McBrayer *et al.* (*39*) evaluated the association of GLUT11 expression and FDG uptake in multiple myeloma. We have observed a significant elevation of GLUT11 expression in both NEPC and NELPC. Similarly, GLUT7 and 8 have high affinity to glucose (*40*) and we observe their amplification in samples with NEGS. Contrary to HK1-3, glucokinase which is known as a glucose sensor in pancreatic beta-cells, is not inhibited by its product glucose-6-phosphate but remains active while glucose is abundant (*37,38*).

We can speculate that the apparent elevation of glucose uptake in NEPC or NELPC could be due to elevation of the expression of the aforementioned high affinity of GLUTs (Supplemental Fig. 26). While our study provides functional support for this conclusion, it is also important to remember the complications associated with a focus on gene expression of this vast family of glucose transport regulators. Avril's commentary (*13*) elaborates on the complex number of molecular, cellular, tissue and organ related variables regulating the resulting ^{18}F-FDG signal, all of which may provide inconsistencies between GLUT expression and the resulting ^{18}F-FDG signal.

GLUT1 is a high affinity and basal glucose transporter expressed ubiquitously in human tissues. In hormone-sensitive PC, GLUT1 gene expression is positively correlated with androgen levels (*41*). Our work implies that GLUT1 expression has limited prognostic potential since it cannot estimate development or existence of low-AR phenotypes such as NEPC or DNPC phenotype. GLUT12 has been recently introduced as a downstream target of AR and its expression is tightly regulated by androgens (*42*). Our data demonstrated the *SLC2A12* suppression is also a highly associated with development of PSMA-low and NE-high gene signature in mCRPC. This work shows *GCK*-amplification and *SLC2A12* suppression correlate with the PSMA-suppression, higher Gleason score and shorter time to biochemical recurrence in NELPC.

For pre-clinical studies, the use of FDG-imaging in mice xenografts can be limited by several factors such as operating cost and short half-life of the radioactive substance and nonradioactive glucose probes, which are of particular interest (*21*). Also, the engraftment of tumors in mice can be challenging to establish and are time-consuming. This work demonstrates the feasibility of non-radioactive imaging of glucose uptake in PC xenografts using a zebrafish model as a rapid and cost-effective model.

CONCLUSION

NEPC, DNPC and NELPC have distinct differential expression of GLUT and HK genes. In accordance with this, the loss of PSMA in NEPC is associated with elevated glucose uptake.

DISCLOSURE

The authors declare no conflict of interest.

KEY POINTS

QUESTION: We investigated whether the expression levels of glucose uptake-associated genes are correlated with development of NEGS and/or suppression of the PSMA gene.

PERTINENT FINDINGS: Data mining approaches, cell lines, mouse and zebrafish PDX models were used to demonstrate that GLUT and HK expression, specially *GCK* and *SCL2A12*, are associated with NEGS, PSMA-suppression and higher glucose uptake.

IMPLICATIONS FOR PATIENT CARE: This study supports the use of FDG-PET for imaging of low-PSMA PC tumors with NEGS.

REFERENCES

1. Stelloo S, Bergman AM, Zwart W. Androgen receptor enhancer usage and the chromatin regulatory landscape in human prostate cancers. *Endocr Relat Cancer.* 2019;26:267–285.

2. Stelloo S, Nevedomskaya E, Kim Y, et al. Integrative epigenetic taxonomy of primary prostate cancer. *Nat Commun.* 2018;9:4900.

3. Bluemn EG, Coleman IM, Lucas JM, et al. Androgen receptor pathway-independent prostate cancer is sustained through FGF signaling. *Cancer Cell.* 2017;32:474–489.

4. Beltran H, Prandi D, Mosquera JM, et al. Divergent clonal evolution of castration resistant neuroendocrine prostate cancer. *Nat Med.* 2016;22:298–305.

5. Alshalalfa M, Liu Y, Wyatt AW, et al. Characterization of transcriptomic signature of primary prostate cancer analogous to prostatic small cell neuroendocrine carcinoma. *Int J Cancer.* 2019;in press.

6. Li Y, Donmez N, Sahinalp C, et al. SRRM4 drives neuroendocrine transdifferentiation of prostate adenocarcinoma under androgen receptor pathway inhibition. *Eur Urol.* 2017;71:68–78.

7. Hope TA, Goodman JZ, Allen IE, et al. Meta-analysis of ^{68}Ga-PSMA-11 PET accuracy for the detection of prostate cancer validated by histopathology. *J Nucl Med.* 2019;60:786-793.

8. Sheikhbahaei S, Afshar-Oromieh A, Eiber M, et al. Pearls and pitfalls in clinical interpretation of prostate-specific membrane antigen (PSMA)-targeted PET imaging. *Eur J Nucl Med Mol Imaging.* 2017;44:2117–2136.

9. Tosoian JJ, Gorin MA, Rowe SP, et al. Correlation of PSMA-targeted (18)F-DCFPyL PET/CT findings with immunohistochemical and genomic data in a patient with metastatic neuroendocrine prostate cancer. *Clin Genitourin Cancer.* 2017;15:65–68.

10. Chakraborty PS, Tripathi M, Agarwal KK, et al. Metastatic poorly differentiated prostatic carcinoma with neuroendocrine differentiation: negative on ^{68}Ga-PSMA PET/CT. *Clin Nucl Med.* 2015;40:163–166.

11. Bakht MK, Derecichei I, Li Y, et al. Neuroendocrine differentiation of prostate cancer leads to PSMA suppression. *Endocr Relat Cancer.* 2019;26:131–146.

12. Haberkorn U, Ziegler SI, Oberdorfer F, et al. FDG uptake, tumor proliferation and expression of glycolysis associated genes in animal tumor models. *Nucl Med Biol* 1994;21:827–834.

13. Avril N. GLUT1 expression in tissue and ^{18}F-FDG uptake. *J Nucl Med.* 2004;45:930–932.

14. Yang H, Zhong JT, Zhou SH, Han HM. Roles of GLUT-1 and HK-II expression in the biological behavior of head and neck cancer. *Oncotarget.* 2019;10:3066–3083.

15. Bozkurt MF, Virgolini I, Balogova S, et al. Guideline for PET/CT imaging of neuroendocrine neoplasms with ^{68}Ga-DOTA-conjugated somatostatin receptor targeting peptides and ^{18}F–DOPA. *Eur J Nucl Med Mol Imaging.* 2017;44:1588–1601.

16. Jadvar H. PET of glucose metabolism and cellular proliferation in prostate cancer. *J Nucl Med.* 2016;57:25–29.

17. Perez PM, Hope TA, Behr SC, et al. Intertumoral heterogeneity of ^{18}F-FDG and ^{68}Ga-PSMA uptake in prostate cancer pulmonary metastases. *Clin Nucl Med.* 2019;44:28–32.

18. Parida GK, Tripathy S, Datta Gupta S, et al. Adenocarcinoma prostate with neuroendocrine differentiation: potential utility of ^{18}F-FDG PET/CT and ^{68}Ga-DOTANOC PET/CT over ^{68}Ga-PSMA PET/CT. *Clin Nucl Med.* 2018;43:248–249.

19. Spratt DE, Gavane S, Tarlinton L, et al. Utility of FDG-PET in clinical neuroendocrine prostate cancer. *Prostate.* 2014;74:1153–1159.

20. Thang SP, Violet J, Sandhu S, et al. Poor outcomes for patients with metastatic castration-resistant prostate cancer with low prostate-specific membrane antigen (PSMA) expression deemed ineligible for ^{177}Lu-labelled PSMA radioligand therapy. *Eur Urol Oncol.* 2018;in press.

21. Cheng Z, Levi J, Xiong Z, et al. Near-infrared fluorescent deoxyglucose analogue for tumor optical imaging in cell culture and living mice. *Bioconjug Chem.* 2006;17:662–669.

22. Lee HY, Lee JJ, Park J, Park SB. Development of fluorescent glucose bioprobes and their application on real-time and quantitative monitoring of glucose uptake in living cells. *Chemistry.* 2011;17:143–150.

23. Melong N, Steele S, MacDonald M, et al. Enzalutamide inhibits testosterone-induced growth of human prostate cancer xenografts in zebrafish and can induce bradycardia. *Sci Rep.* 2017;7:14698.

24. Taylor BS, Schultz N, Hieronymus H, et al. Integrative genomic profiling of human prostate cancer. *Cancer Cell.* 2010;18:11–22.

25. Tsai HK, Lehrer J, Alshalalfa M, Erho N, Davicioni E, Lotan TL. Gene expression signatures of neuroendocrine prostate cancer and primary small cell prostatic carcinoma. *BMC Cancer.* 2017;17:759.

26. Subramanian A, Tamayo P, Mootha VK, et al. Gene set enrichment analysis: a knowledge-based approach for interpreting genome-wide expression profiles. *Proc Natl Acad Sci U S A* 2005;102:15545–15550.

27. Akamatsu S, Wyatt AW, Lin D, et al. The placental gene PEG10 promotes progression of neuroendocrine prostate cancer. *Cell Rep.* 2015;12:922-936.

28. Korbel GA, Lalic G, Shair MD. Reaction microarrays: a method for rapidly determining the enantiomeric excess of thousands of samples. *J Am Chem Soc.* 2001;123:361–362.

29. Park J, Lee HY, Cho MH, Park SB. Development of a Cy3-labeled glucose bioprobe and its application in bioimaging and screening for anticancer agents. *Angew Chem Int Ed Engl.* 2007;46:2018–2022.

30. Park J, Um JI, Jo A, et al. Impact of molecular charge on GLUT-specific cellular uptake of glucose bioprobes and in vivo application of the glucose bioprobe, GB2-Cy3. *Chem Comm.* 2014;50:9251–9254.

31. Ding Y, Li Y, Lu L, et al. Inhibition of nischarin expression promotes neurite outgrowth through regulation of PAK activity. *PLOS ONE.* 2015;10:e0144948.

32. Dunning MJ, Vowler SL, Lalonde E, et al. Mining human prostate cancer datasets: The "camcAPP" Shiny App. *EBioMedicine.* 2017;17:5–6.

33. Yuan T-C, Veeramani S, Lin F-F, et al. Androgen deprivation induces human prostate epithelial neuroendocrine differentiation of androgen-sensitive LNCaP cells. *Endocr Relat Cancer.* 2006;13:151–167.

34. Qian Y, Wang X, Chen X. Inhibitors of glucose transport and glycolysis as novel anticancer therapeutics. *World J Transl Med.* 2014;3:37–57.

35. Choi SYC, Ettinger SL, Lin D, et al. Targeting MCT 4 to reduce lactic acid secretion and glycolysis for treatment of neuroendocrine prostate cancer. *Cancer Med.* 2018;7:3385–3392.

36. Li W, Cohen A, Sun Y, et al. The role of CD44 in glucose metabolism in prostatic small cell neuroendocrine carcinoma. *Mol Cancer Res.* 2016;14:344-353.

37. McKerrecher D, Waring MJ. Chapter one - Property-based design in the optimisation of benzamide glucokinase activators: from hit to clinic. In: Lawton G, Witty DR, eds. *Prog Med Chem.* Vol 52: Elsevier; 2013:1–43.

38. Roberts DJ, Miyamoto S. Hexokinase II integrates energy metabolism and cellular protection: akting on mitochondria and TORCing to autophagy. *Cell Death Differ.* 2015;22:364.

39. McBrayer SK, Cheng JC, Singhal S, Krett NL, Rosen ST, Shanmugam M. Multiple myeloma exhibits novel dependence on GLUT4, GLUT8, and GLUT11: implications for glucose transporter-directed therapy. *Blood.* 2012;119:4686–4697.

40. Gonzalez-Menendez P, Hevia D, Mayo JC, Sainz RM. The dark side of glucose transporters in prostate cancer: Are they a new feature to characterize carcinomas? *Int J Cancer.* 2018;142:2414–2424.

41. Vaz CV, Marques R, Alves MG, et al. Androgens enhance the glycolytic metabolism and lactate export in prostate cancer cells by modulating the expression of GLUT1, GLUT3, PFK, LDH and MCT4 genes. *J Cancer Res Clin Oncol.* 2016;142:5–16.

42. White MA, Tsouko E, Lin C, et al. GLUT12 promotes prostate cancer cell growth and is regulated by androgens and CaMKK2 signaling. *Endocr Relat Cancer.* 2018;25:453–469.

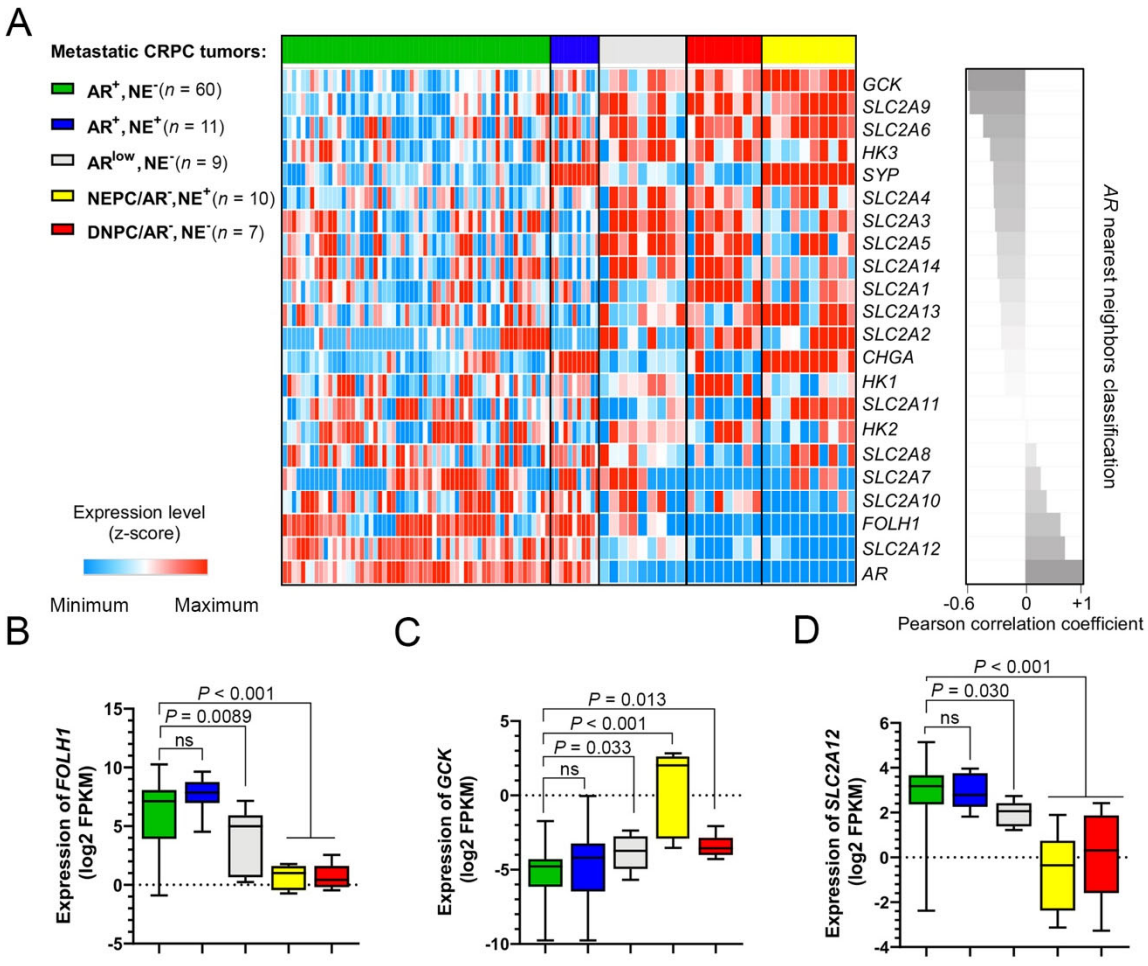

FIGURE 1. AR-negative subsets of mCRPC in UW cohort (*3*) have suppressed expression of *FOLH1* and differential expression of *SLC2A* and *HKs* genes. (A) The heatmap plot of the expression levels of *SLC2A* family members, *HK* genes, *AR*, *FOLH1* and NE-markers sorted based on nearest neighbors clustering to *AR*. (B-D) The box-whisker plots show the expression of *FOLH1*, *SLC2A12* and *GCK*.

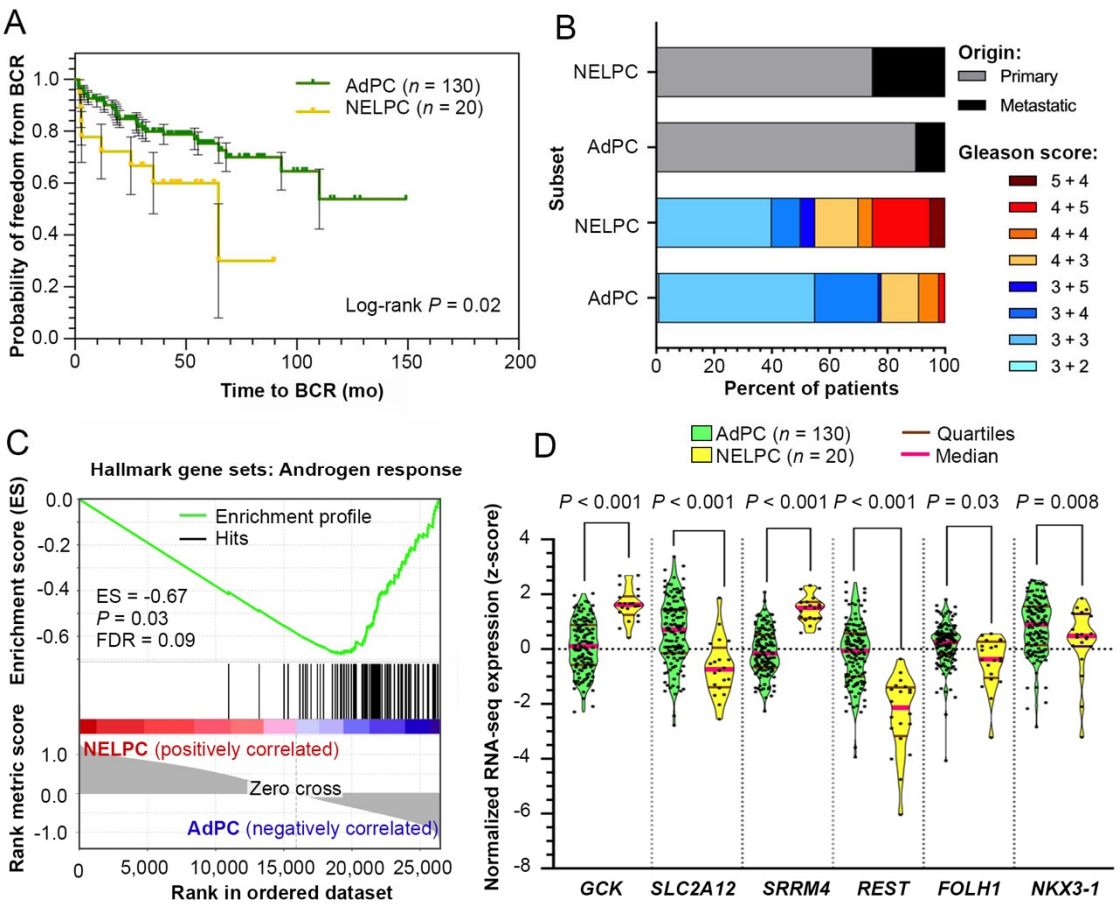

FIGURE 2. The NELPC subset of MSKCC cohort (*24*) displays (A) shorter time to BCR, (B) more prevalence of metastatic and high Gleason score specimens and (C) lack of AR response. Violin plots compare the distribution of *SLC2A12*, *GCK* and *FOLH1*expressions in NELPC and AdPC subsets. BCR = biochemical recurrence.

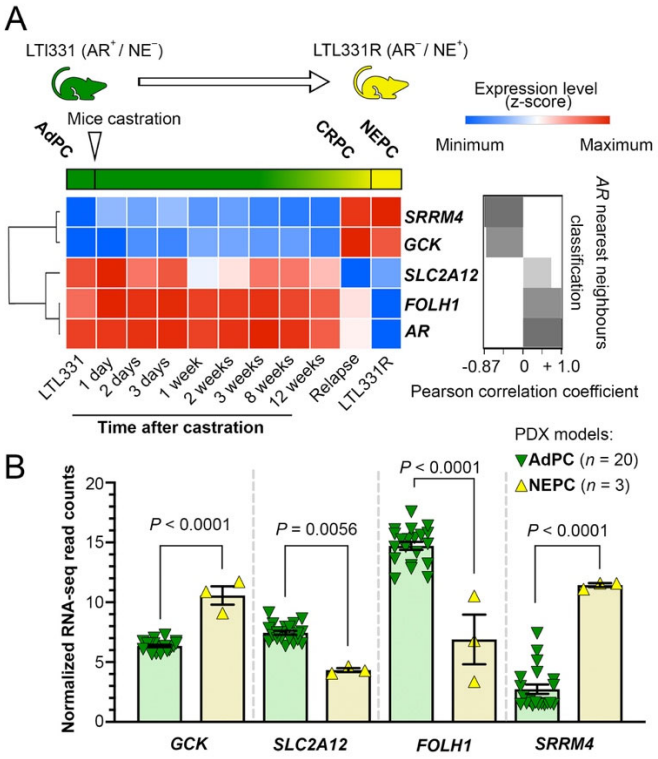

FIGURE 3. NEPC PDX models have suppressed expression of *FOLH1* and differential expressions of *SLC2A12* and *GCK*. (A) Transcription of the studied genes during progression to NEPC and correlation with *AR*. (B) The expression of the studied genes in PDX models.

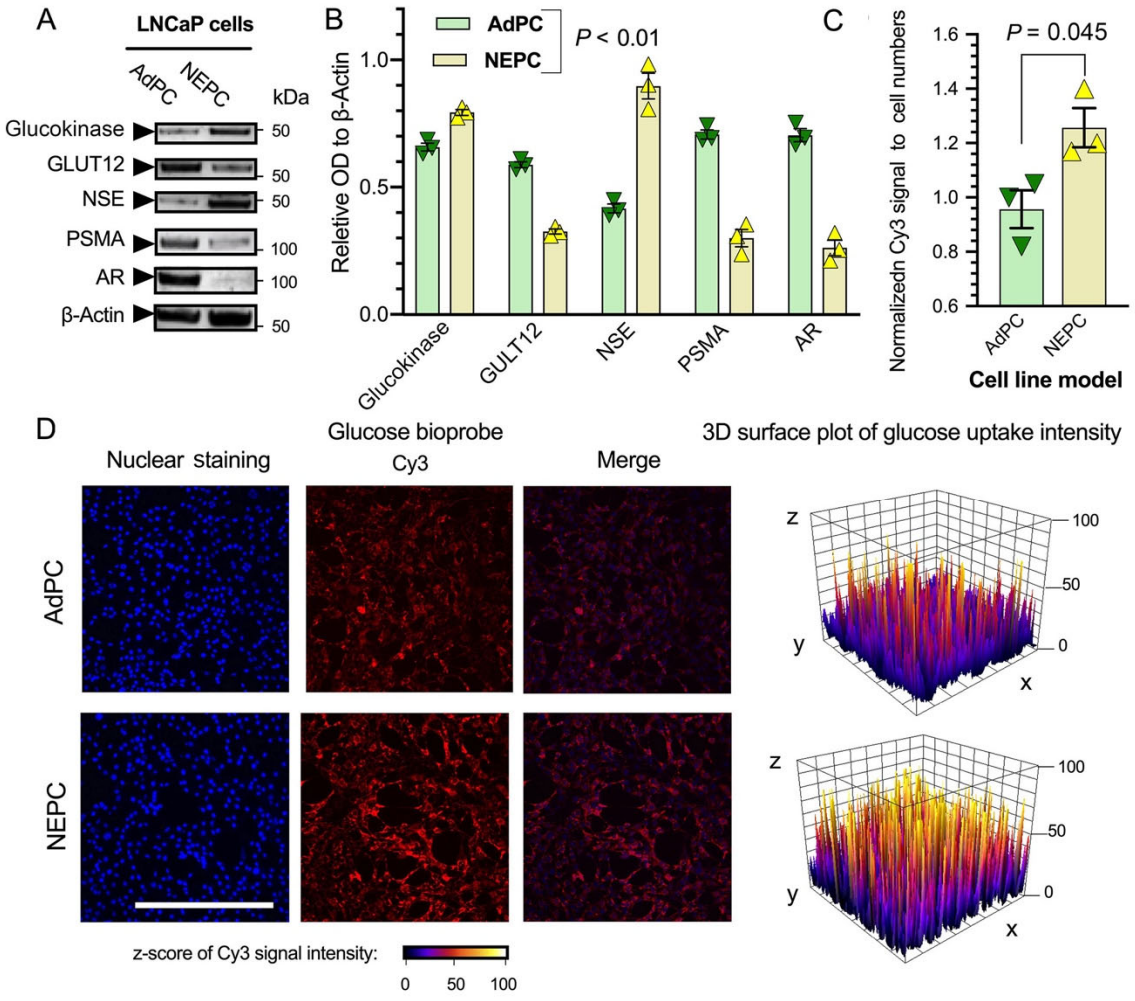

FIGURE 4. The NE-induced LNCaP cell line represents higher glucose uptake and differential protein levels of glucokinase and GLUT12. (A-B) Western blot analyses of protein levels. (C-D) Quantification of GB2-Cy3 uptake and representative images of LNCaP cells. Scale bar = 200 microns.

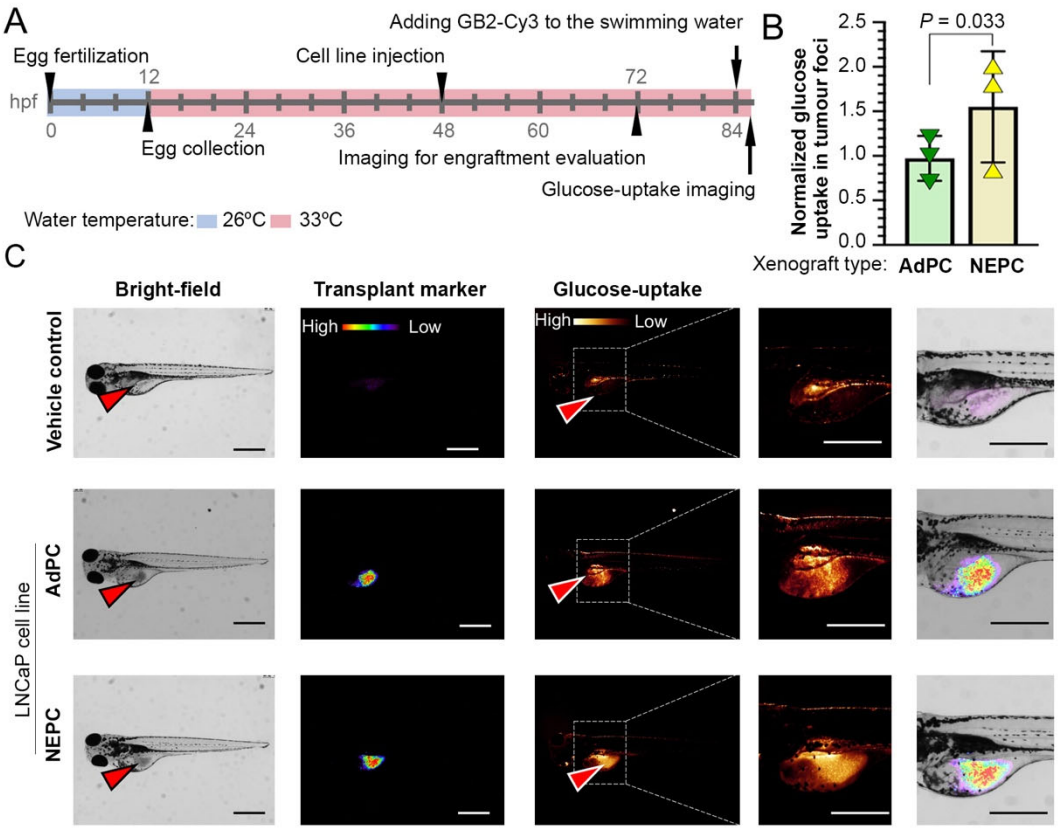

FIGURE 5. The NE-induced LNCaP cell line xenografts represent higher glucose uptake in a zebrafish model. (A) Schematic of the experiment. (B-C) Quantification of GB2-Cy3 uptake and representative images of embryos injected with different LNCaP cells. Red arrows show the injection sites. Scale bar = 200 microns.

SUPPLEMENTAL MATERIAL

GB2-Cy3 Glucose Bioprobe Synthesis

Solvents were purchased from Caledon Laboratories (Caledon, Ontario), Sigma-Aldrich (Oakville, Ontario), or VWR Canada (Mississauga, Ontario). Other chemicals were purchased from Sigma-Aldrich, AK Scientific, Oakwood Chemicals, Alfa Aesar, or Acros Chemicals and were used without further purification unless otherwise noted. Anhydrous toluene, tetrahydrofuran (THF), diethyl ether, and *N*,*N*-dimethylformamide (DMF) were obtained from an Innovative Technology (Newburyport, United States) solvent purification system based on aluminum oxide columns. CH_2Cl_2, and acetonitrile were freshly distilled from CaH_2 prior to use. Purified water was obtained from a Millipore deionization system. All heated reactions were conducted using oil baths on IKA RET Basic stir plates equipped with a P1000 temperature probe. Thin layer chromatography was performed using EMD aluminum-backed silica 60 F254-coated plates and visualized using either UV-light (254 nm), $KMnO_4$, vanillin, Hanessian's stain, or Dragendorff's stain. Preparative TLC was done using glass-backed silica plates (Silicycle) of either 250, 500, 1000, or 2000 μm thickness depending on application. Column chromatography was carried out using standard flash technique with silica (Silicycle Siliaflash-P60, 230−400 mesh) under compressed air pressure. Standard workup procedure for all reactions undergoing an aqueous wash involved back extraction of every aqueous phase, drying of the combined organic phases with anhydrous magnesium sulfate, filtration either using vacuum and a sintered-glass frit or through a glass-wool plug using gravity, and concentration under reduced pressure on a rotary evaporator (Buchi or Synthware). ^{1}H Nuclear magnetic

resonance (NMR) spectra were obtained at 300 or 500 MHz, and ^{13}C NMR spectra were obtained at 75 or 125 MHz on Bruker instruments. NMR chemical shifts (δ) are reported in ppm and are calibrated against residual solvent signals of $CHCl_3$ (δ 7.26), DMSO-d_5 (δ 2.50) or methanol-d_3 (δ 3.31). HRMS analyses were conducted on a Waters XEVO G2-XS TOF instrument with an ASAP probe in CI mode. Supplemental Scheme 1 illustrates the required steps for synthesis of the conjugatable dye Cy3-OH.

Compound (100): (2-bromoethyl)-D-glucoside

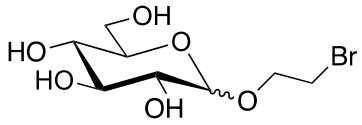

To a solution of glucose (5 g, 27.75 mmol) in 2-bromoethanol (30 mL, 0.417 mol) was added Dowex 50WX8-400 hydrogen form ion-exchange resin (5 g; the resin was washed with MeOH before use) and the reaction mixture was refluxed at 70 °C for 16 h and the reaction completion was monitored by TLC (2:1, ethyl acetate: hexanes). The reaction mixture was filtered to remove the resin, poured into methanol (10 mL) and dried ($MgSO_4$). The resulting solution was filtered and concentrated under reduced pressure. After purification of the glycosylated compound by silica gel flash column chromatography (1:1, ethyl acetate: hexanes), the desired compound was obtained as a mixture of α and β anomers (6.24 g. 78% yield). The analytical data were consistent with the literature values (*1*).

Compound (101): (2-Bromoethyl)-2,3,4,6-tetra-*O*-benzoyl-α-D-glucoside

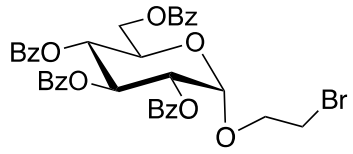

Compound 100 (1.89 g, 6.58 mmol) was dissolved in a mixture of pyridine (40 mL) and 4-DMAP (81 mg, 0.66 mmol) at 0 °C. Benzoyl chloride (6.1 mL, 53 mmol) was then added dropwise and the resulting mixture was allowed to warm to room temperature with stirring for 16 h. The mixture was quenched by the addition of methanol (10 mL) and subsequently extracted with ethyl acetate (3 × 20 mL); the combined organic extracts were washed with 1 M HCl (2 × 10 mL), saturated sodium bicarbonate (1 × 10 mL), and brine (1 × 10 mL). The organic layer was dried ($MgSO_4$), filtered and the solvent removed under reduced pressure. The resulting oil was purified using silica-gel chromatography (3:1 hexanes/ethyl acetate) to give **compound 101** (3.4 g, 74% yield). The analytical data were consistent with the literature values (*1*).

Compound (102): [2-(*N*-Boc-piperazynoethyl)]-2,3,4,6-tetra-*O*-benzoyl-α-D-glucoside

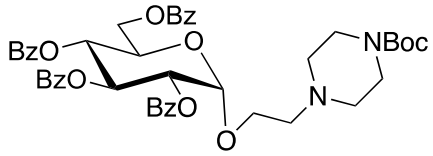

To a solution of **Compound 101** (1 g, 1.42 mmol) in 15 mL anhydrous DMF was added *N*-Boc-piperazine (529 mg, 2.84 mmol), potassium iodide (426 mg, 2.84 mmol) and Et_3N (593 μL, 4.26 mmol), and the resultant mixture was stirred at 80 °C for 10 h. After the reaction was complete, as monitored by TLC, the solution was diluted with water (10 mL),

extracted with ethyl acetate (3 × 20mL) and the combined organic layers washed with brine (1 × 20 mL). The organic layer was dried ($MgSO_4$) and concentrated under reduced pressure. The desired product was purified by silica-gel chromatography (95:3:2, $CHCl_3$: EtOH: Et_3N) to furnish a light yellow crystalline powder (680 mg, 59% yield). The analytical data was consistent with the literature values (*1*).

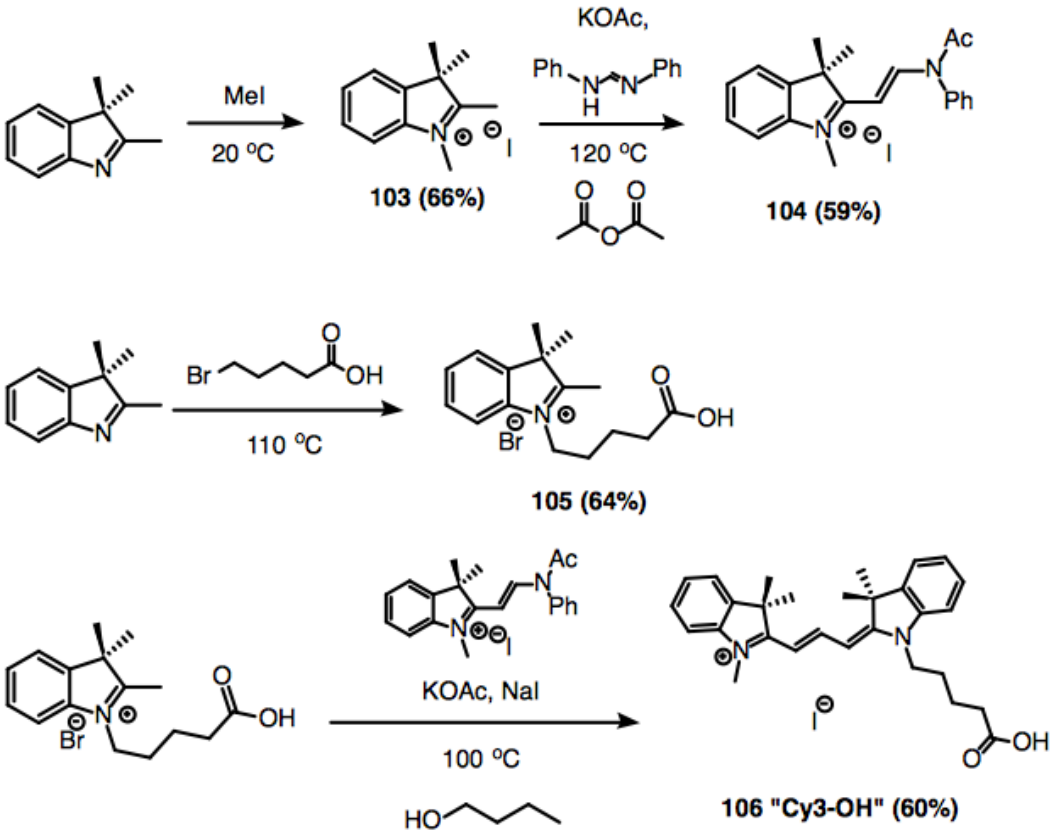

Supplemental scheme 1. Overview of the synthesis of the conjugatable dye Cy3-OH.

Compound (103): 1,2,3,3-tetramethyl-3*H*-indolium iodide

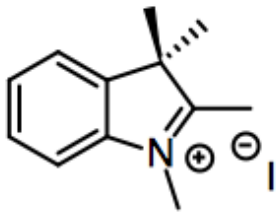

To a 0.3 M solution of 2,3,3-trimethylindolenine (5 mL, 31.15 mmol) in MeCN (104 mL), was added iodomethane (2.23 mL, 37.38 mmol) and the reaction was stirred at room temperature for 16 h, resulting in a pale pink precipitate. The precipitate was filtered and rinsed with Et_2O (3 × 10 mL) to afford compound **103** (5.1 g, 54% yield). The analytical data were consistent with the literature.

Compound (104): (*E*)-1,3,3-trimethyl-2-(2-(*N*-phenylacetamido)vinyl)-3*H*-indolium iodide

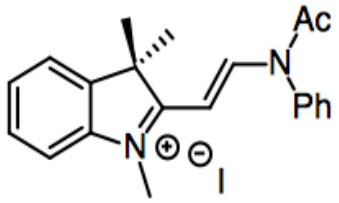

As per reference *(2)*: To 1,2,3,3-tetramethyl-3*H*-indolium iodide, **103**, (3 g, 9.96 mmol), *N*,*N*′-diphenylformamidine (2.44 g, 12.45 mmol), and potassium acetate (98 mg, 0.996 mmol) was added 22.5 mL acetic anhydride and the mixture was heated for 5 h at 120 °C. The reaction was then allowed to cool to room temperature and the red precipitate was collected by filtration. The precipitate was washed repeatedly with Et_2O until the filtrate was colorless providing compound **104** (2.7 g, 59%). R_f = 0.81 (DCM : MeOH = 4 : 1). The ^1H NMR was consistent with the literature: ^1H-NMR (500 MHz, $CDCl_3$, 23 °C) δ 9.19-9.16 (d, *J* = 14.2 Hz, 1H); 3.86 (s, 3H); 2.11 (s, 3H); 1.83 (s, 6H) ppm (*2*).

Compound (105): 1-(4-Carboxybutyl)-2,3,3-trimethyl-3*H*-indolium bromide

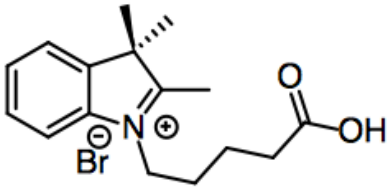

As per reference (*2*): To 5-bromovaleric acid (4.74 g, 26.17 mmol) was added 2,3,3-trimethylindolenine (4 mL, 24.92 mmol) and the neat reaction was stirred for 20 h at 110 °C. The reaction completion was determined when the solution had become a dark red solid and would no longer stir. The crude solid was ground up with a pestle and mortar to create a fine powder. The powder was placed on top of a filter paper in a Buchner funnel and was rinsed with boiling EtOAc (6 × 30 mL), boiling acetone (2 × 30 mL), and boiling acetone (2 × 90 mL) to yield compound **105** (5.43 g, 64%) as an off-white, pink powder. R_f = 0.12 (DCM/MeOH = 3:1). The ^{1}H NMR was consistent with the literature: ^{1}H NMR (500 MHz, CD_3OD + 1 drop D_2O, 23 °C) 7.90-7.87 (m, 1H); 7.78-7.75 (m, 1H); 7.67-7.63 (m, 2H); 4.56-4.52 (t, *J* = 7.7 Hz, 2H); 2.44-2.40 (t, *J* = 7.0 Hz, 2H); 2.04-1.96 (m, 2H); 1.80-1.72 (m, 2H); 1.61 (s, 6H) ppm (*2*).

Compound (106): 1-[(4″-(1″-Carboxybutyl))]-1′,3,3,3′,3′-pentamethyl-indocarbocyanine iodide, "Cy3-OH," (*2*)

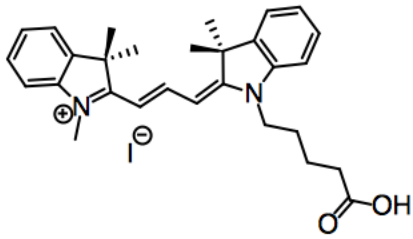

As per reference (*2*): To a flame-dried flask containing **104** (0.73 g, 1.59 mmol), **105** (0.54 g, 1.59 mmol), and potassium acetate (0.156 g, 1.905 mmol) was added anhydrous 1-butanol under a nitrogen atmosphere (*2*). The solution was stirred at 100 °C for 1.5 h. NaI (4.58 g, 30.53 mmol) was then added to the flask and the reaction was stirred at 100 °C for a further 1 h. The reaction was cooled to room temperature and a precipitate formed

overnight. The precipitate was filtered using a Buchner funnel and then rinsed repeatedly using Et_2O until the filtrate was colorless. The precipitate was collected and dissolved in DCM to give a dark purple solution. The crude mixture was purified by silica-gel flash column chromatography using a gradient elution starting at 9:1 DCM/MeOH (v/v) to 4:1 DCM/MeOH (v/v) to give the title compound **106** (543 mg, 60% yield). R_f = 0.66 (4:1 DCM/MeOH). λ_{max} 546 nm.[27] The ^{1}H NMR was consistent with the literature ^{1}H NMR (500 MHz, $CDCl_3$, 23 °C) δ 8.34-8.27 (dd, *J* = 14, 13 Hz, 1H); 7.35-7.29 (m, 4H); 7.22-7.16 (m, 2H); 7.11-7.07 (m, 2H); 6.78 (dd, *J* = 14 Hz, J = 14 Hz, 2H); 4.13 (bt, 2H); 3.71 (s, 3H); 2.47 (bt, 2H); 1.85 (m, 4H); 1.65 (s, 6H) .

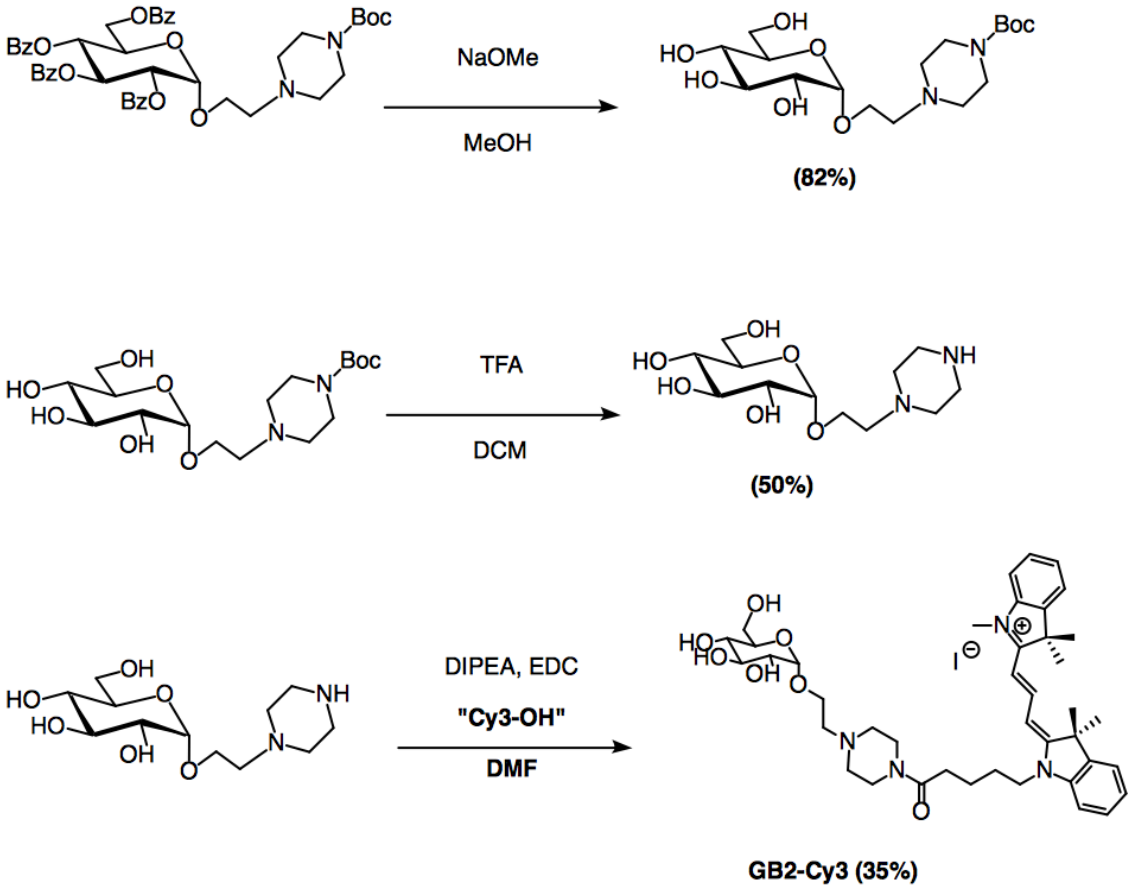

Supplemental scheme 2. Synthetic strategy for the preparation of GB2-Cy3

Compound (107): *Tert*-butyl-4-(2-(((2*S*,3*R*,4*S*,5*S*,6*R*)-3,4,5-trihydroxy-6-(hydroxymethyl)tetrahydro-2*H*-pyran-2-yl)oxy)ethyl)piperazine-1-carboxylate

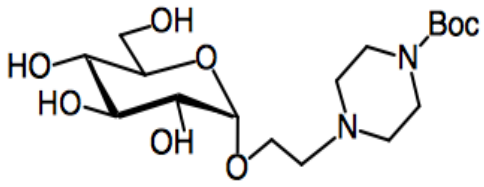

As per reference (*3*): To a solution of **104** (66.4 mg, 0.0821 mmol) in MeOH (3.3 mL) was added MeONa (~0.5 M in MeOH, 1.22 mL, 0.611 mmol) and the reaction completion was determined by TLC (100% MeOH). After the reaction was complete, the mixture was neutralized with Dowex 50WX8-400 hydrogen form ion-exchange resin (1 scoop the size of a pea), and then concentrated under reduced pressure. The residue was dissolved in a minimal amount of MeOH and the methyl benzoate ester was removed using a silica plug (25 mL SiO_2) washed with three 25 mL portions of Et_2O. Between each Et_2O portion, the filtrate was monitored by TLC to ensure only the methyl benzoate was being eluted (R_f = 0.9 to 1.0, 100% Et_2O). Unlike reference (*3*), the compound was isolated. The desired compound, **107,** was then eluted using MeOH (25 mL) and the solvent removed under reduced pressure (26.4 mg, 82% yield). The ^{1}H NMR was consistent with the expected spectrum (*3*).

Compound (108): (2*R*,3*S*,4*S*,5*R*,6*S*)-2-(hydroxymethyl)-6-(2-(piperazin-1-yl)ethoxy)tetrahydro-2*H*-pyran-3,4,5-triol (*3*).

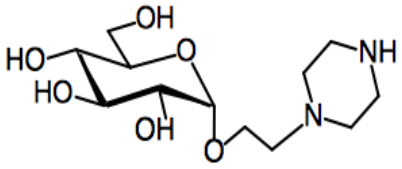

As per reference (*3*): 1:1 Trifluoroacetic acid (5.5 mL, excess) in DCM (5.5 mL) was added to compound **107** (50 mg, 0.1274 mmol) for 1 h followed by evaporation and purging with nitrogen. Unlike reference (*3*), the

compound was isolated. The resulting residue was washed with toluene (3 × 5 mL) and decanted to remove any residual TFA. Any residual toluene was removed under reduced pressure to give compound **108** (18.6 mg, 50% yield). The ^{1}H NMR was consistent with the expected spectrum (*3*).

Compound (109): GB2-Cy3

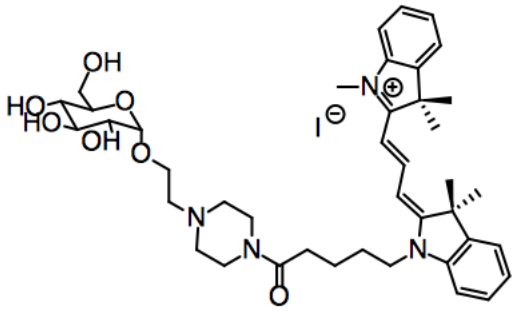

As per reference (*1*) with modifications: Compound **108** (20 mg, 0.0684 mmol) in DMF (300 µL) was slightly basified with DIPEA (20 µL) and Cy3-OH (**106**) (30.3 mg, 0.0684 mmol) and EDC (7 mg, 0.046 mmol) added as a solution in DMF (50 µL). The reaction mixture was stirred at room temperature for 2 h and the reaction was monitored by TLC. The resulting solution was purified by prep high performance liquid chromatography (HPLC) and the elution protocol is as listed: 1) 95% eluent A and 5% eluent B for 5 min, 2) linear gradient to 60% eluent A (40% B) over 4 min, 3) linear gradient to 50% eluent A (50% B) over 10 min, 4) linear gradient to 5% eluent A (95% B) over 10 min, 5) linear gradient to 0% eluent A (100% B) over 5 min, 6) constant flow with 0% eluent A (100% B) for 10 min, and 7) linear gradient to 95% eluent A (5% B) over 10 min for regeneration and washing of the column. Retention time = 12 min, scanning for a λ_{max} 546 nm to give **GB2-Cy3 (109)** (17 mg, 35% yield). The ^{1}H NMR was consistent with the literature: ^{1}H NMR (500 MHz, CD_3OD) δ 8.55 (t, *J* = 13.5 Hz, 1H), 7.54 (d, *J* = 7.5 Hz, 2H), 7.47–7.30 (m, 6H), 6.45 (dd, *J* = 13.4, 9.0 Hz, 2H), 4.20–4.17 (m, 2H), 4.08–4.05 (m, 1H), 3.83–3.80 (m, 3H), 3.67 (s, 3H) 3.63–3.42 (m, 12H),

2.57–2.54 (m, 2H), 1.97–1.79 (m, 6H), 1.78 (s, 6H), 1.77 (s, 6H) ppm (*1*). Supplemental Scheme 2 summarizes the synthetic strategy of GB2-Cy3.

NMR spectrum of compound 101-106 are presented on Supplemental Figs. 16-22. HPLC spectrum of GB2-Cy3 is illustrated on Supplemental Fig. 23.

GB2-Cy3 *in vitro* imaging of glucose uptake

For *in vitro* imaging for glucose uptake by GB2-Cy3 we adopted published protocols (*1*). Briefly, 50,000 LNCaP cells were seeded in 12 well glass-bottom dishes (Corning) overnight at 37°C. Cells were washed 2 times with PBS and incubated for 1 hour at 37°C in glucose-deficient DMEM medium. Cells were treated with 7 μg/mL GB2-Cy3 and 100 ng/mL Hoechst 33342 (Thermo Scientific) in glucose-deficient DMEM at 37 °C for 5, 10 and 30 minutes, respectively. Cells were washed twice with PBS and prepared for live imaging by adding 1 mL of PBS. Fluorescence images were obtained on a LeicaDM IL microscope (Wetzlar, Germany). Cy3 signal was quantified using ImageJ and the mean fluorescent signal measurement from 30–40 cells.

***In Vivo* Glucose Uptake Imaging**

In vivo uptake of GB2-Cy3 in was visualized by modifications of previous protocols (*4,5*). Full experimental details are provided in the Supplemental Material.

Eggs were collected after fertilization and kept at 33°C for 48 hours post-fertilization (hpf). Three hours before implantation, attached LNCaP cells were incubated with 100 ng/mL Hoechst 33342 for 40 minutes at 37°C. After staining, cells were rinsed twice with PBS and RPMI-10% CSS medium was added.

At 48 hpf embryos were anesthetised with 0.168 mg/mL of Tricaine (Sigma, MS222). 100-150 labelled cells/ 9 nL were loaded into glass capillary needles and injected into the yolk sac of each embryo using a Nanoject II (Fisher Scientific). After injection, embryos were kept in water at 33°C. At 72 hpf the xenograft was examined using a Leica fluorescent stereoscope. 84 hpf embryos were treated with 250 μg/mL GB2-Cy3 at 33°C for 2 hours, followed by a water wash and a 15 minutes incubation. Embryos were then anesthetized, and imaged. Fold change in tumour foci and glucose uptake were quantified by total DAPI and Cy3 fluorescence respectively. The image for each embryo was imported into ImageJ, converted to a 32-bit greyscale, and the threshold was adjusted to eliminate background pixels.

REFERENCE FOR SUPPLEMENTAL MATERIAL

1. Lee HY, Lee JJ, Park J, Park SB. Development of fluorescent glucose bioprobes and their application on real-time and quantitative monitoring of glucose uptake in living cells. *Chemistry.* 2011;17:143-150.

2. Korbel GA, Lalic G, Shair MD. Reaction microarrays: a method for rapidly determining the enantiomeric excess of thousands of samples. *J Am Chem Soc.* 2001;123:361-362.

3. Park J, Lee HY, Cho MH, Park SB. Development of a Cy3-labeled glucose bioprobe and its application in bioimaging and screening for anticancer agents. *Angew Chem Int Ed Engl.* 2007;46:2018-2022.

4. Park J, Um JI, Jo A, et al. Impact of molecular charge on GLUT-specific cellular uptake of glucose bioprobes and in vivo application of the glucose bioprobe, GB2-Cy3. *Chem Comm.* 2014;50:9251-9254.

5. Melong N, Steele S, MacDonald M, et al. Enzalutamide inhibits testosterone-induced growth of human prostate cancer xenografts in zebrafish and can induce bradycardia. *Sci Rep.* 2017;7:14698.

Supplemental figure 1.

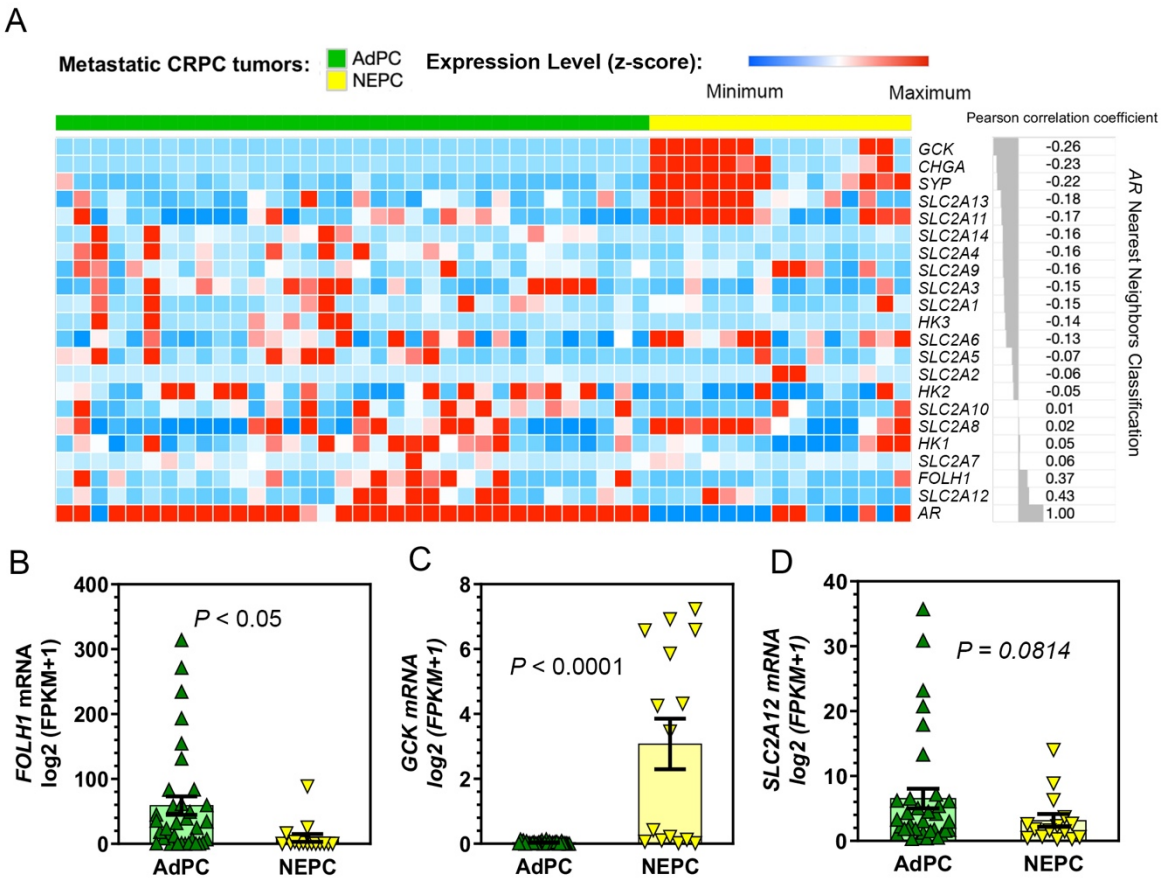

NEPC samples of the Beltran cohort (*1*) have suppressed *FOLH1* and differential *SLC2A12* and *GCK* expression. (A) Heatmap plot of the expression levels of *SLC2A* family members, *HK* genes, *AR*, *FOLH1*and NE-markers sorted based on nearest neighbors clustering to AR. (B-D) The mean expression of *FOLH1*, *GCK* and *SLC2A12* in metastatic CRPC samples. Error bars reflect SEM and Student's t-test was performed.

Supplemental figure 2.

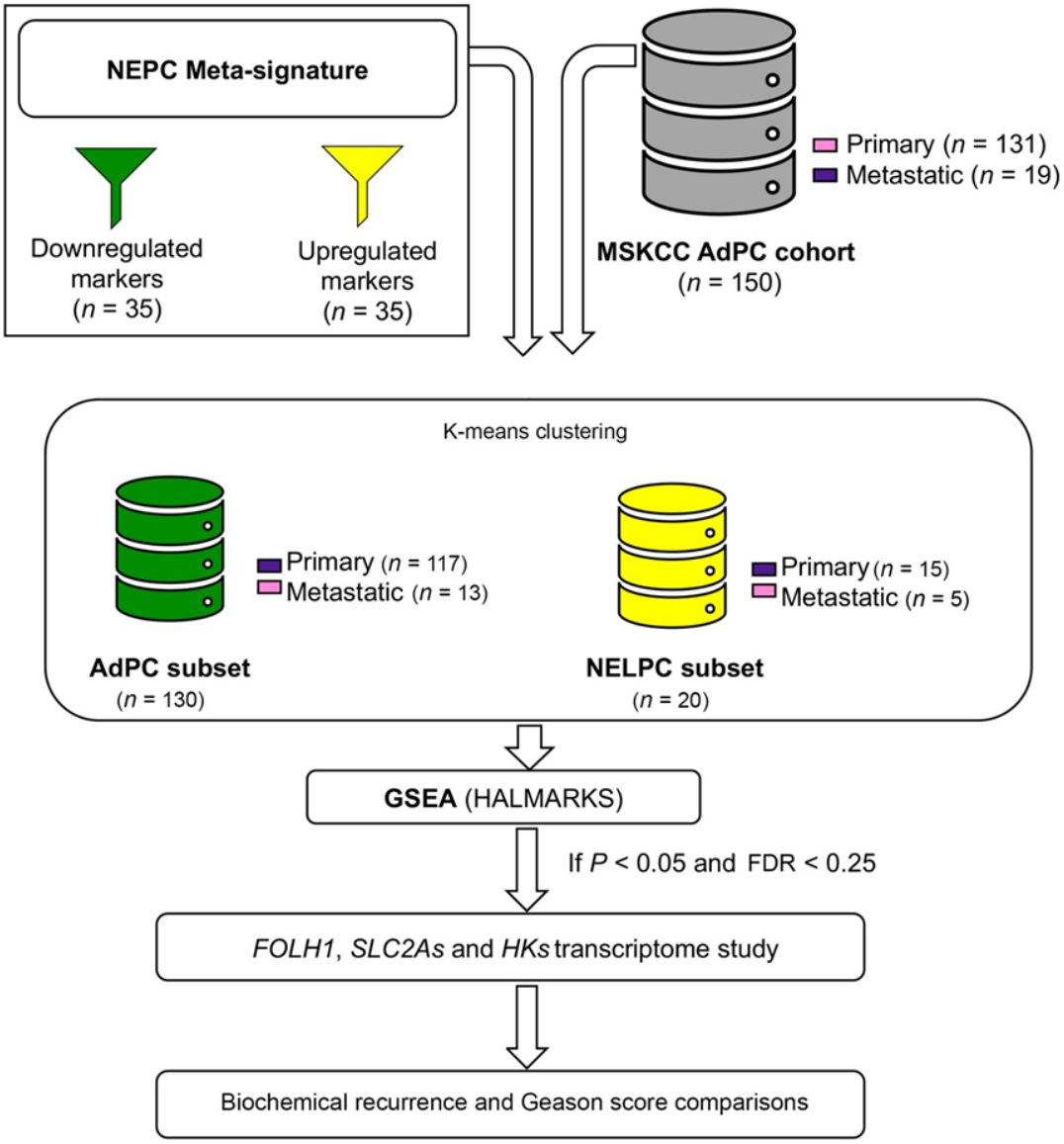

A schematic of the process used to identify a NELPC subset among a population of metastatic and primary AdPC samples. The meta-signature of prototypical high-grade NEPC (*2*) was used to identify a potential NELPC subset among the AdPC MSKCC cohort (*3*). This meta-signature consists of two sets of markers for classification of AdPC and NEPC. GSEA was used to confirm that the identified subset is characteristic of a low-AR hallmark. FDR = False discovery rate. GSEA = Gene set enrichment analysis

Supplemental figure 3.

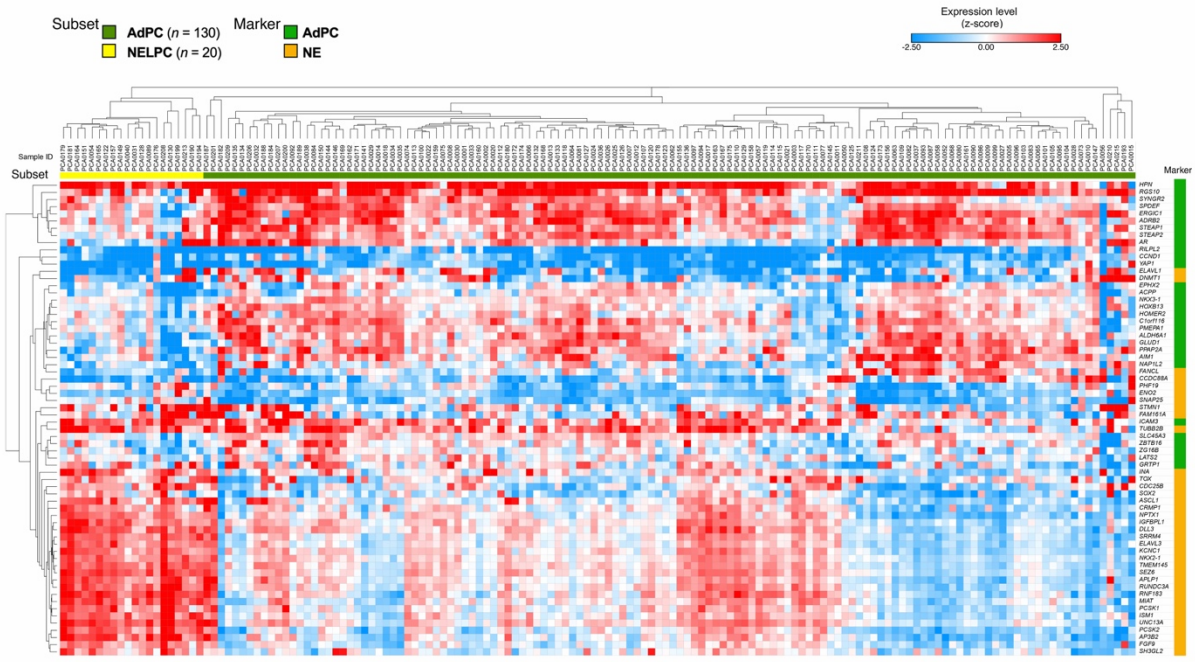

Heatmap showing the expression of NEPC markers in the NELPC subset identified from MSKCC cohort (*3*).

Supplemental figure 4.

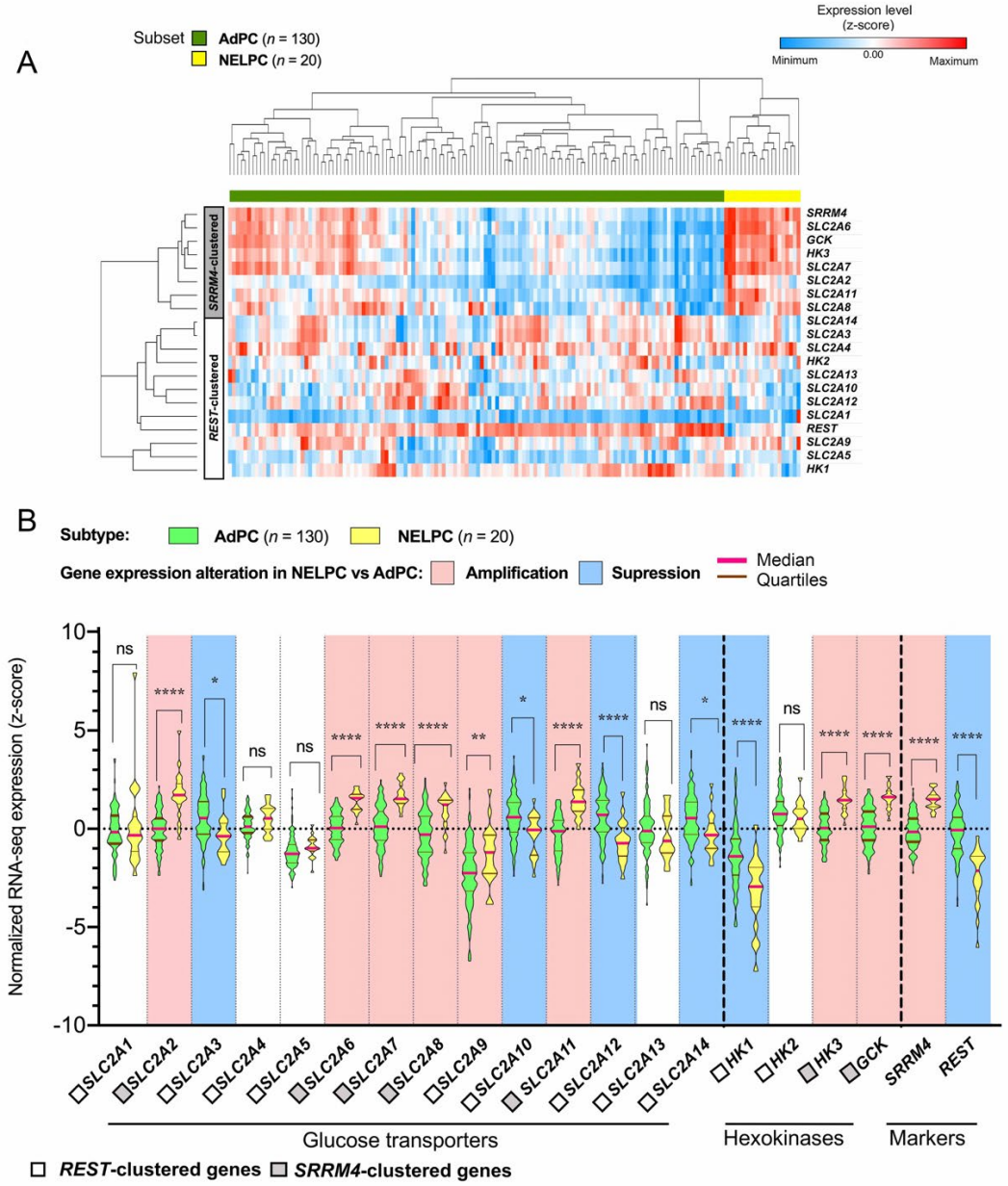

Amplification of *SRRM4*-clustered *SLC2A* and *HK* genes in NELPC subset of patients in MSKCC cohort (*3*). (A) Heatmap plot of the mean expression levels of *SLC2A* family members, *HK* genes, *REST* as AdPC marker and *SRRM4* as NE marker. (B) Violin plots compare the distribution of *SLC2As* and *HK*s expressions in NELPC and AdPC subsets.

Supplemental figure 5.

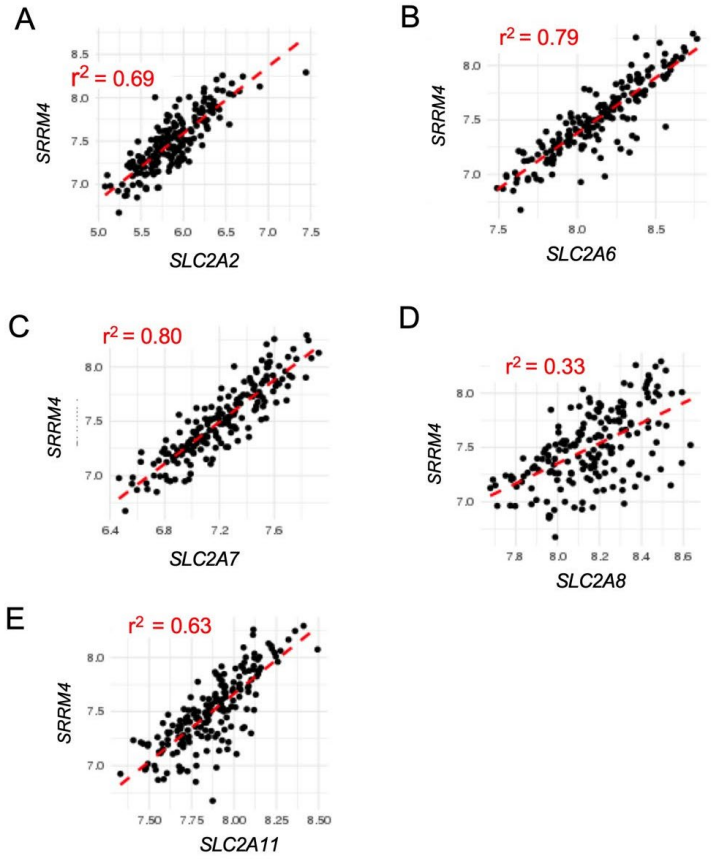

SLC2A2, 6-8, 11 genes are co-expressed with *SRRM4* as a treatment induced NEPC marker. (A-E) Pairwise-correlation of *SRRM4* and the introduced *SRRM4*-clustered *SLC2A* gene expression followed by Pearson correlation analysis generated using MSKCC PC cohort data (*3*).

Supplemental figure 6.

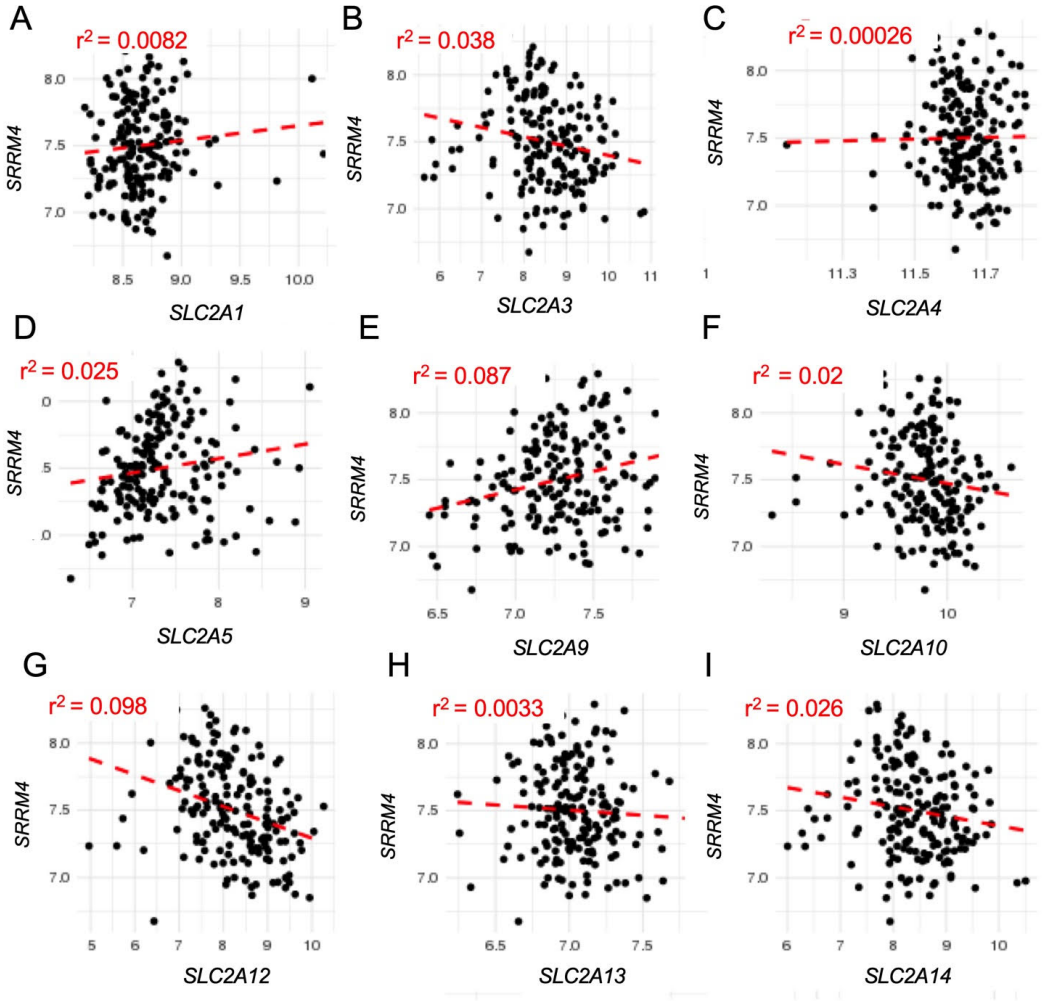

SLC2A1, 3-5, 9-12 genes *as REST*-clustered genes are not co-expressed with *SRRM4* as a treatment induced NEPC marker. (A-I) Pairwise-correlation of *SRRM4* and the introduced *REST*-clustered *SLC2A* gene expression followed by Pearson correlation analysis generated using MSKCC PC cohort data (*3*).

Supplemental figure 7.

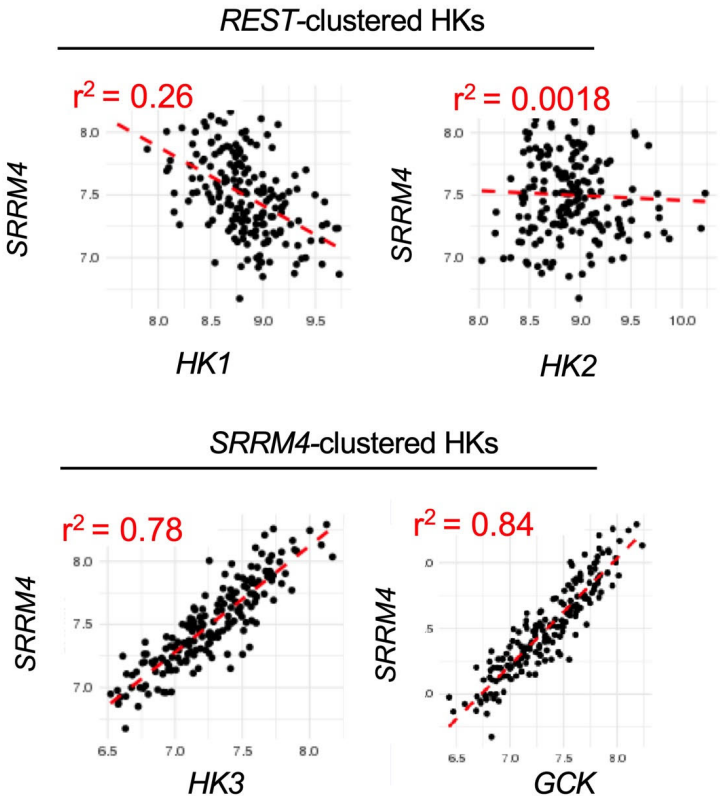

Pairwise-correlation of SRRM4 and HK gene expression followed by Pearson correlation analysis generated using MSKCC PC cohort data (*3*).

Supplemental figure 8.

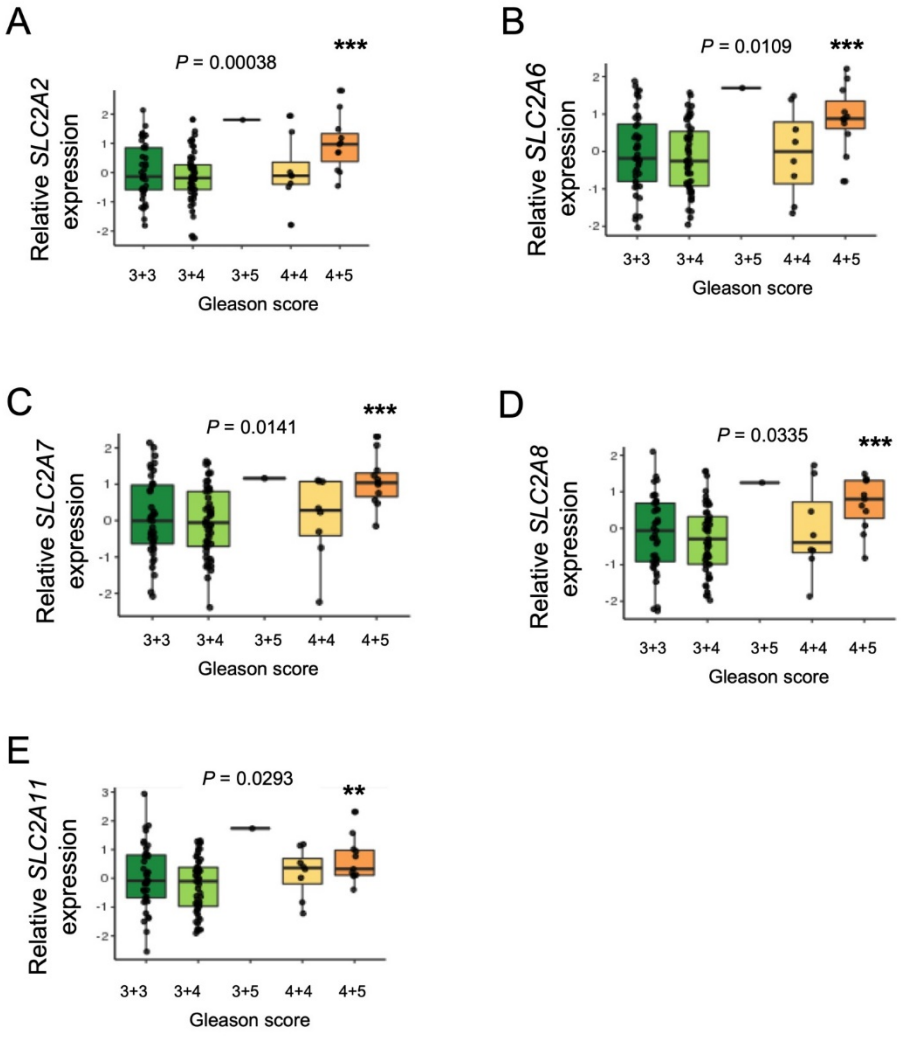

High levels of *SRRM4*-clustered *SLC2A* gene expression are correlated with higher Gleason scores. (A-E) Box-whisker plots showing the expression of *SRRM4*-clustered *SLC2A* genes during progression of AdPC based on Gleason score using MSKCC PC cohort data (*3*). One-way ANOVA followed by unpaired t-tests were performed with Benjamini–Hochberg adjustment for multiple test correction; **: $P < 0.01$ and ***: $P < 0.001$.

Supplemental figure 9.

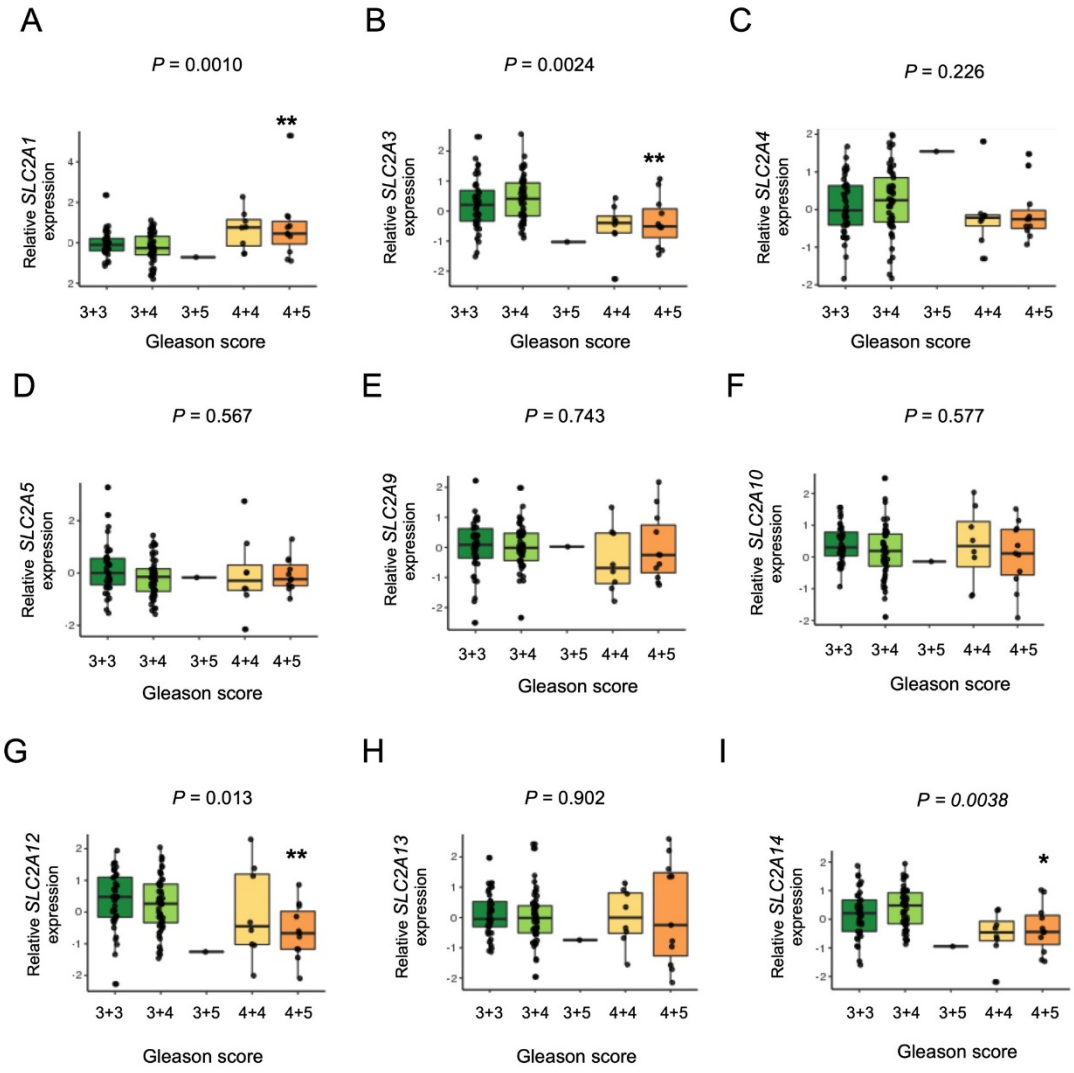

Except *SLC2A1* gene, the high levels of *REST*-clustered *SLC2A* gene expressions do not correlate with higher Gleason scores. (A-I) Box-whisker plots showing the expression of *REST*-clustered *SLC2A* genes during progression of AdPC based on Gleason score using MSKCC PC cohort data (*3*). One-way ANOVA followed by unpaired t-tests were performed with Benjamini–Hochberg adjustment for multiple test correction; *: $P < 0.05$ **: $P < 0.01$.

Supplemental figure 10.

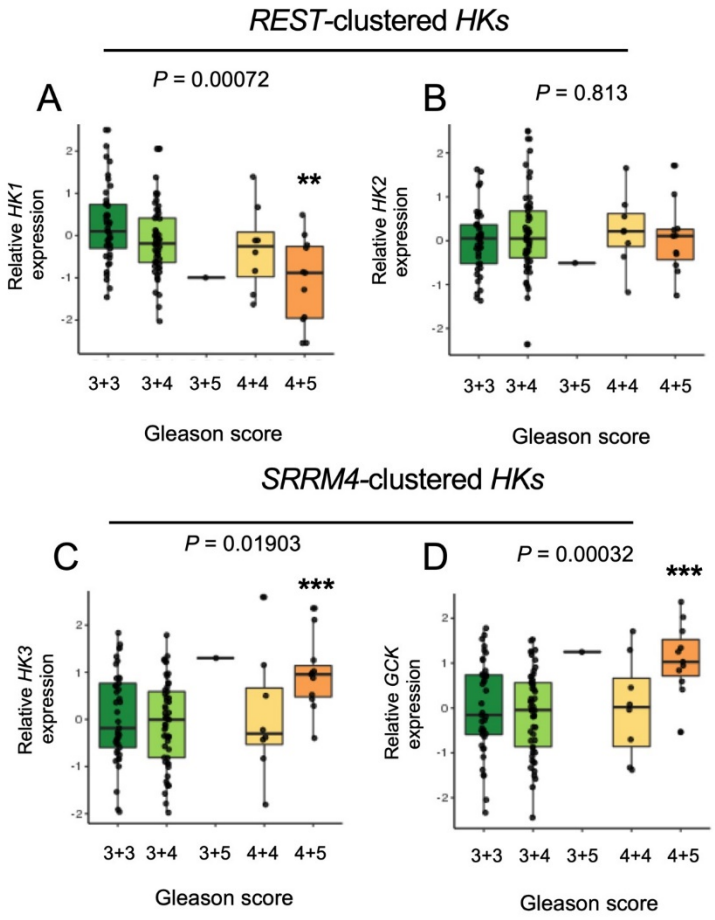

High levels of *SRRM4*-clustered *HK* gene expression are associated with higher Gleason scores. (A-D) Box-whisker plots showing the expression of *HK* genes during progression of AdPC based on Gleason score using MSKCC PC cohort data (*3*). One-way ANOVA followed by unpaired t-tests were performed with Benjamini–Hochberg adjustment for multiple test correction; $^{**}P < 0.01$; $^{***}P < 0.001$.

Supplemental figure 11.

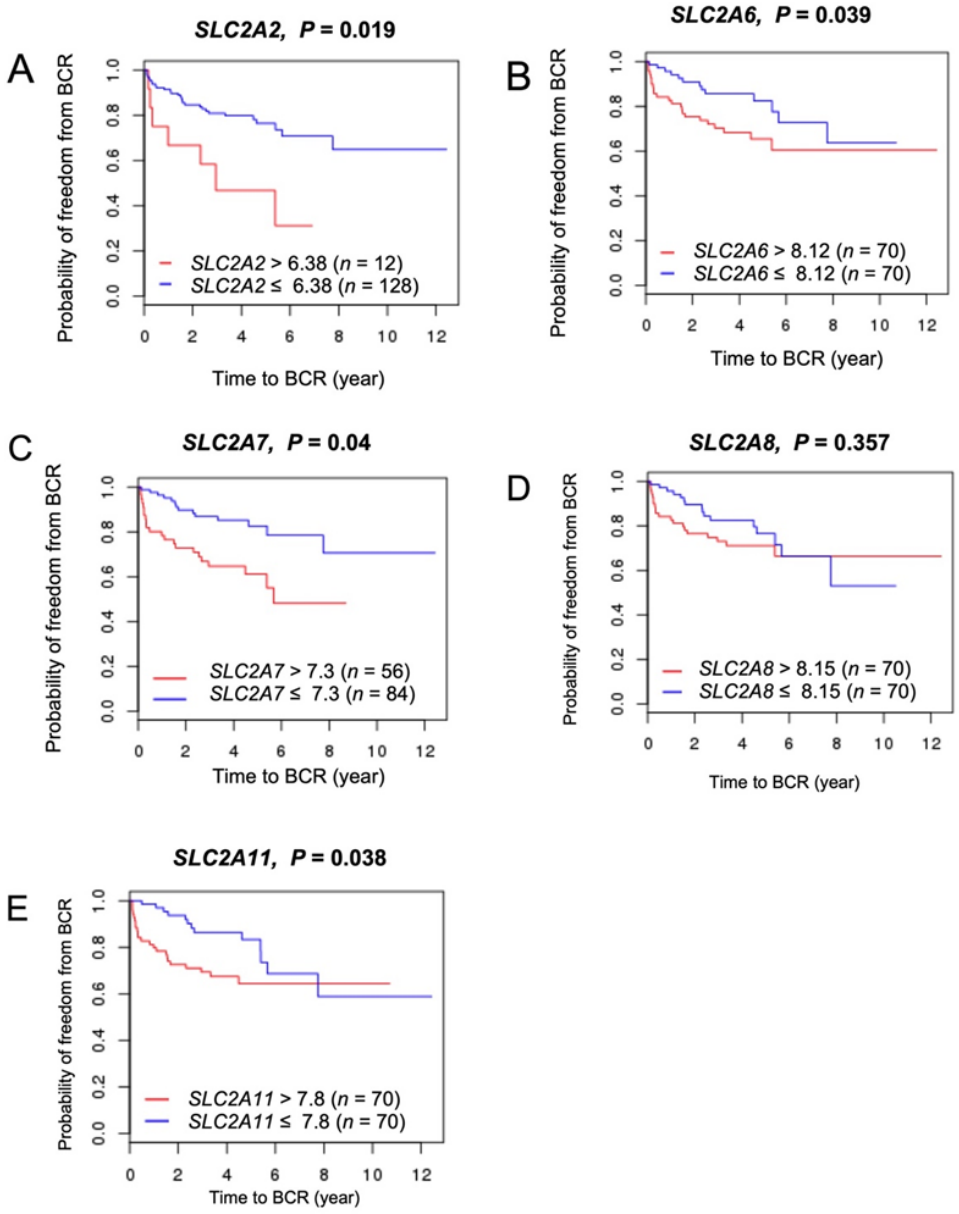

High levels of *SRRM4*-clustered *SLC2A* genes including the expression of *SLC2A2, SLC2A6, SLC2A7* and *SLC2A11* are associated with shorter time to BCR. (A-E) Kaplan-Meyer survival curves for high and low expression levels of *SRRM4*-clustered *SLC2A* genes generated using MSKCC PC cohort data (*3*). The log-rank test was employed to identify statistical difference between the high and low expressing groups. BCR = biochemical recurrence.

Supplemental figure 12.

-

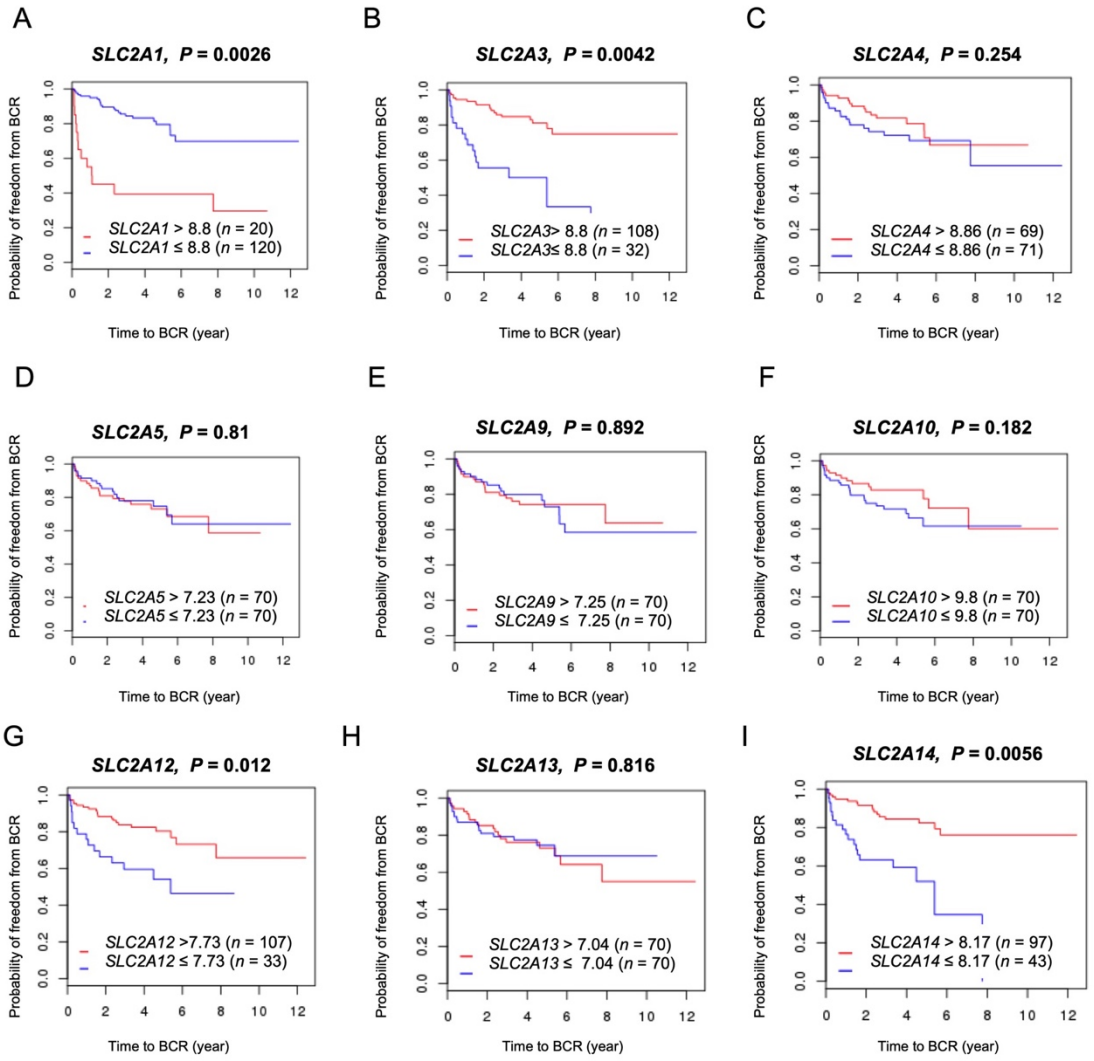

Low levels of *REST*-clustered *SLC2A* genes including *SLC2A3, SLC2A12* and *SLC2A14* expression are associated with shorter time to BCR. (A-I) Kaplan-Meyer survival curves for high and low expression levels of *REST*-clustered *SLC2A* genes generated using MSKCC PC cohort data (*3*). The log-rank test was employed to identify statistical difference between the high and low expressing groups. BCR = Biochemical recurrence.

Supplemental figure 13.

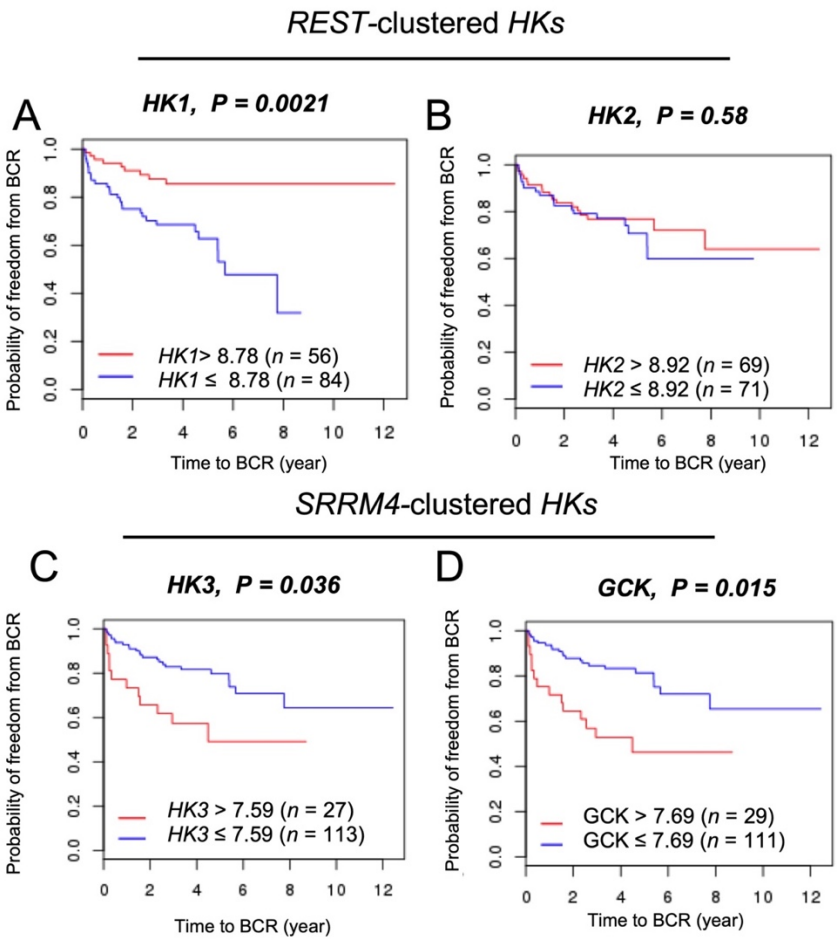

High levels of *SRRM4*-clustered *HK* gene expressions are associated with shorter time to BCR. (A-E) Kaplan Meyer survival curves for high and low expression levels of *HK* genes generated using MSKCC PC cohort data (*3*). The log-rank test was employed to identify statistical difference between the high and low expressing groups. BCR = biochemical recurrence.

Supplemental figure 14.

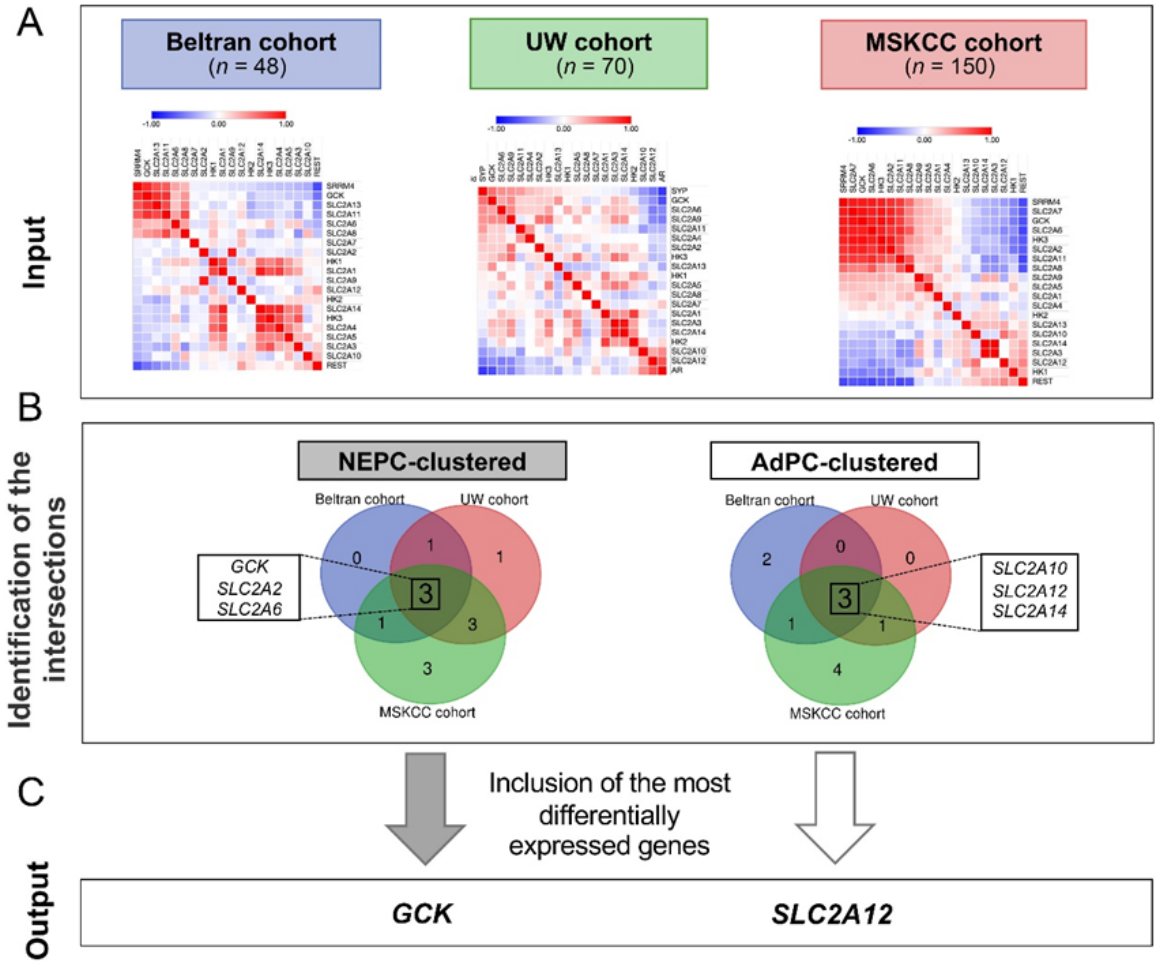

Among *SLC2A* family members and *HK* genes, *GCK* is the most highly expressed gene and *SLC2A12* is the most highly supressed gene in samples with NE gene signature in comparison with samples with an AdPC signature. (A-C) The schematic showing the process of selecting the most differentially expressed genes. (A) The RNA-seq data from 268 prostate cancer samples from MSKCC (*3*), Beltran (*1*) and UW (*4*) cohorts are used to stratify *SLC2A1-14* and *HK1-4* genes into NEPC-clustered and AdPC-clustered groups. (B) Venn diagram illustrating the intersections between the clustered genes in different cohorts. (C) The most highly differentially expressed genes in the intersections are selected to be studied in cell lines and PDX models.

Supplemental figure 15.

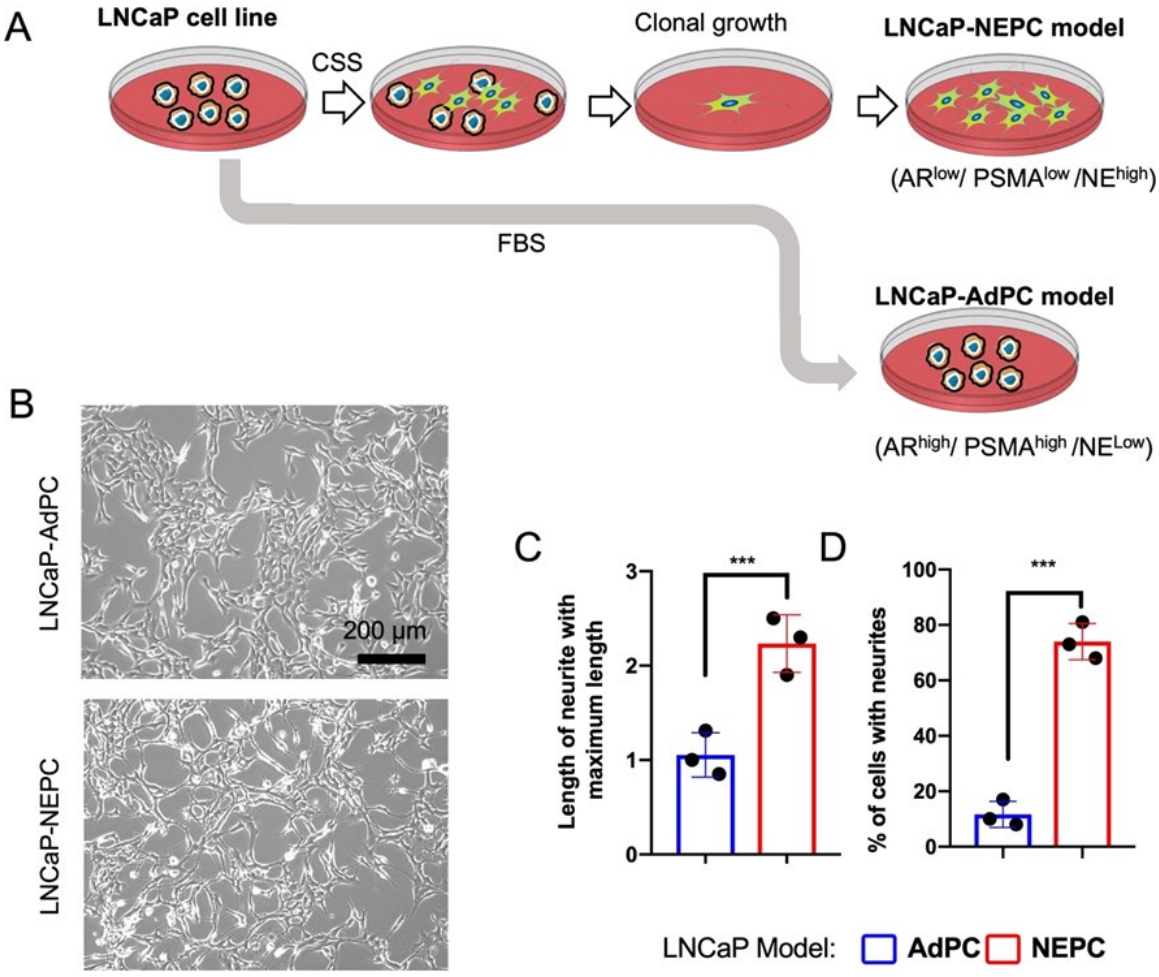

Development of a NE-induced LNCaP cell line. (A) The Schematic showing the steps for progression of the LNCaP cell line to NEPC. (B) Representative photos of control (top) and CSS-treated (bottom) LNCaP cells. (C) Neurites were measured using ImageJ software and longest neurite calculated. (D) % of cells with neurites counted over 3 fields of view. The results are expressed as the mean ± SEM. Differences between two groups were compared by unpaired Student's t-test. ***: $P < 0.001$. Some elements of this figure were produced using Servier Medical Art image bank (www.servier.com). FBS = Fetal bovine serum; CSS = Charcoal- stripped serum.

Supplemental figure 16.

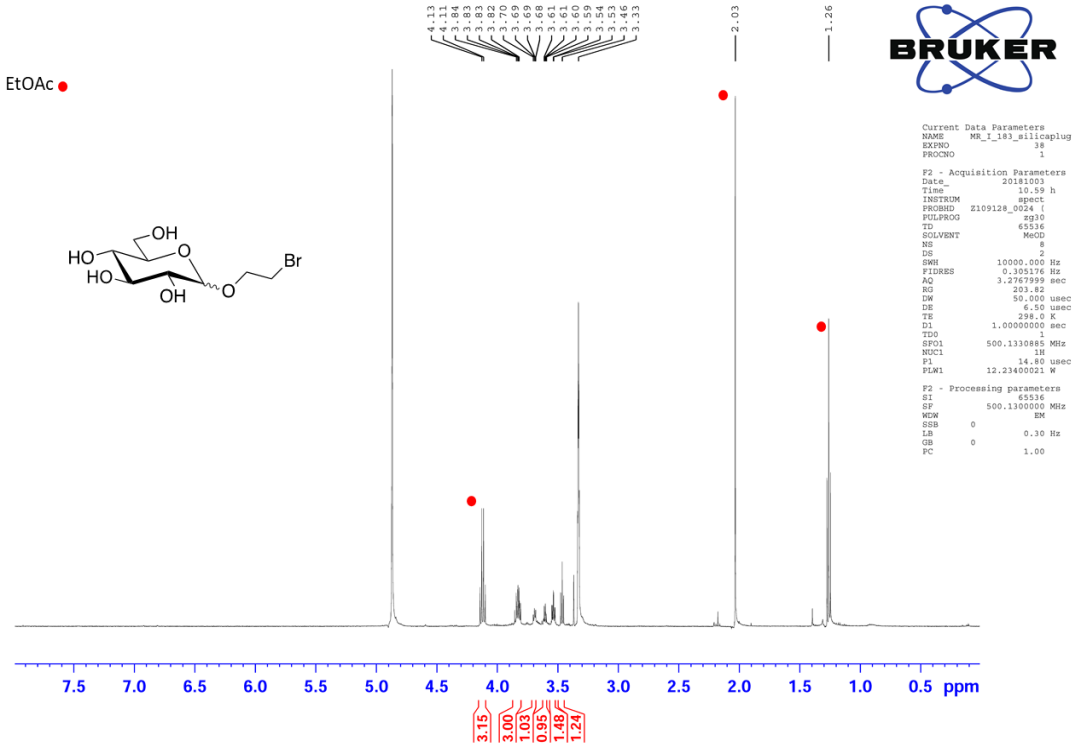

^{1}H NMR spectrum of functionalized glucose (compound 100) with a minimum of 85% α-anomer. NMR = Nuclear magnetic resonance.

Supplemental figure 17.

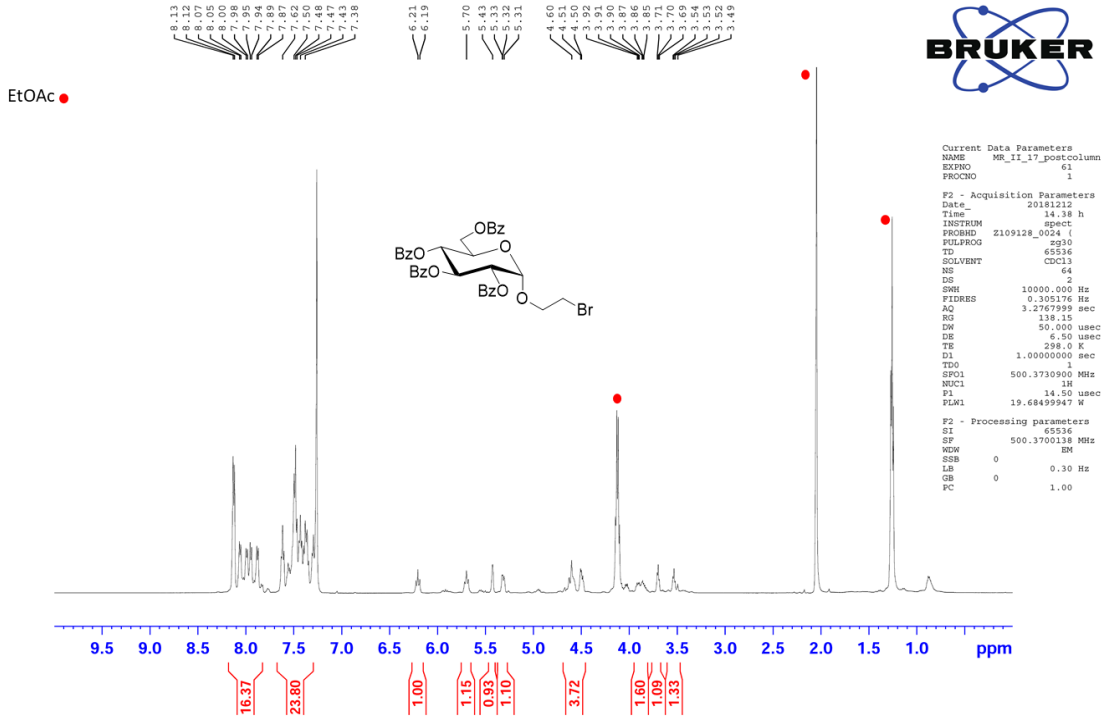

^{1}H NMR spectrum of protected functionalized glucose (compound 101). NMR = Nuclear magnetic resonance.

Supplemental figure 18.

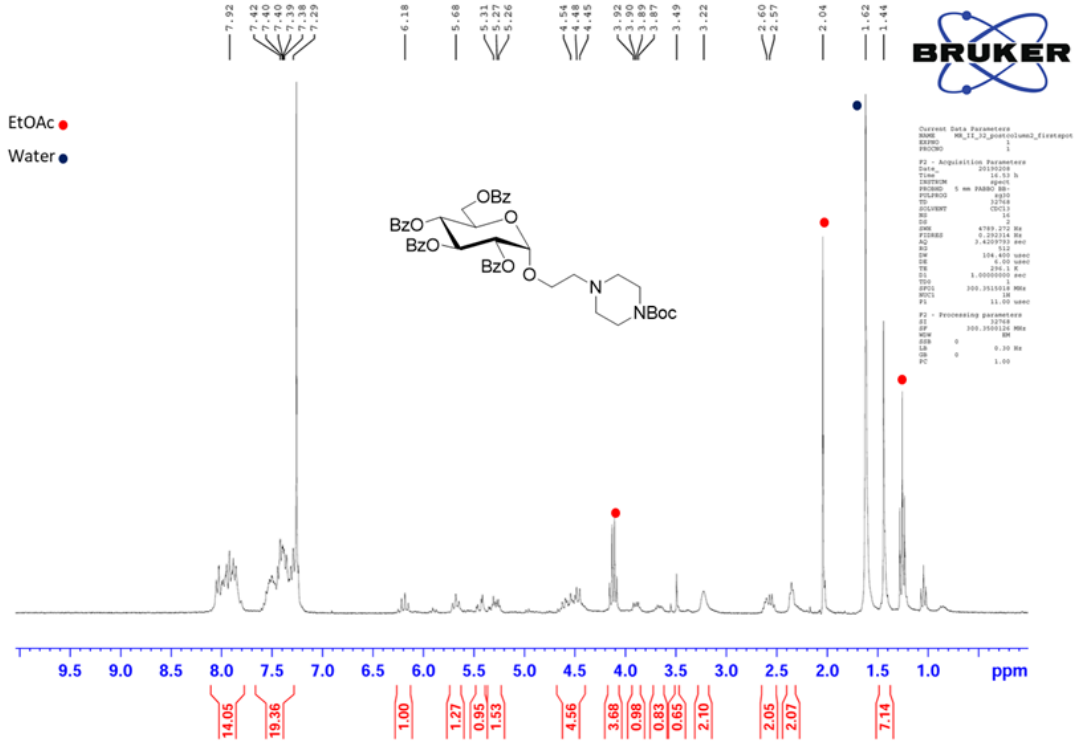

^{1}H NMR spectrum of piperazine-functionalized glucose (compound 102). NMR = Nuclear magnetic resonance.

Supplemental figure 19.

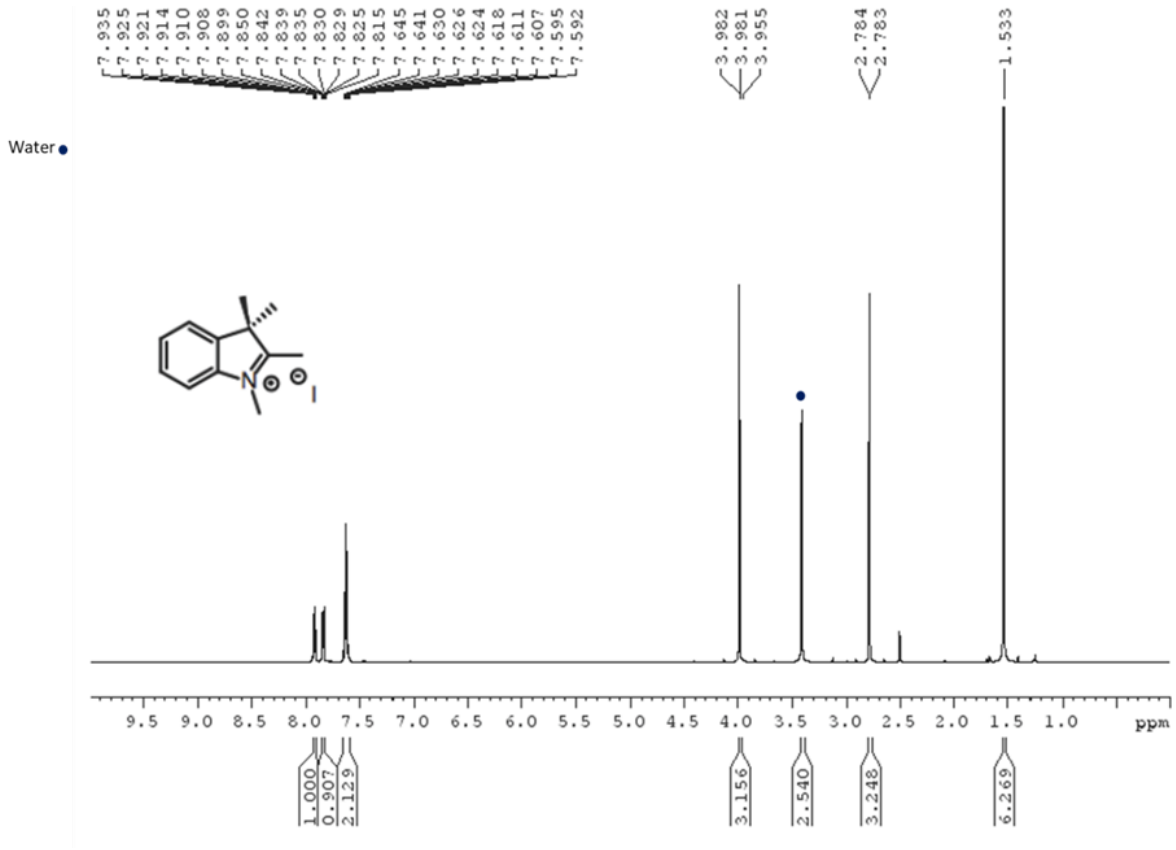

^{1}H NMR spectrum of indolium salt (compound 103). NMR = Nuclear magnetic resonance.

Supplemental figure 20.

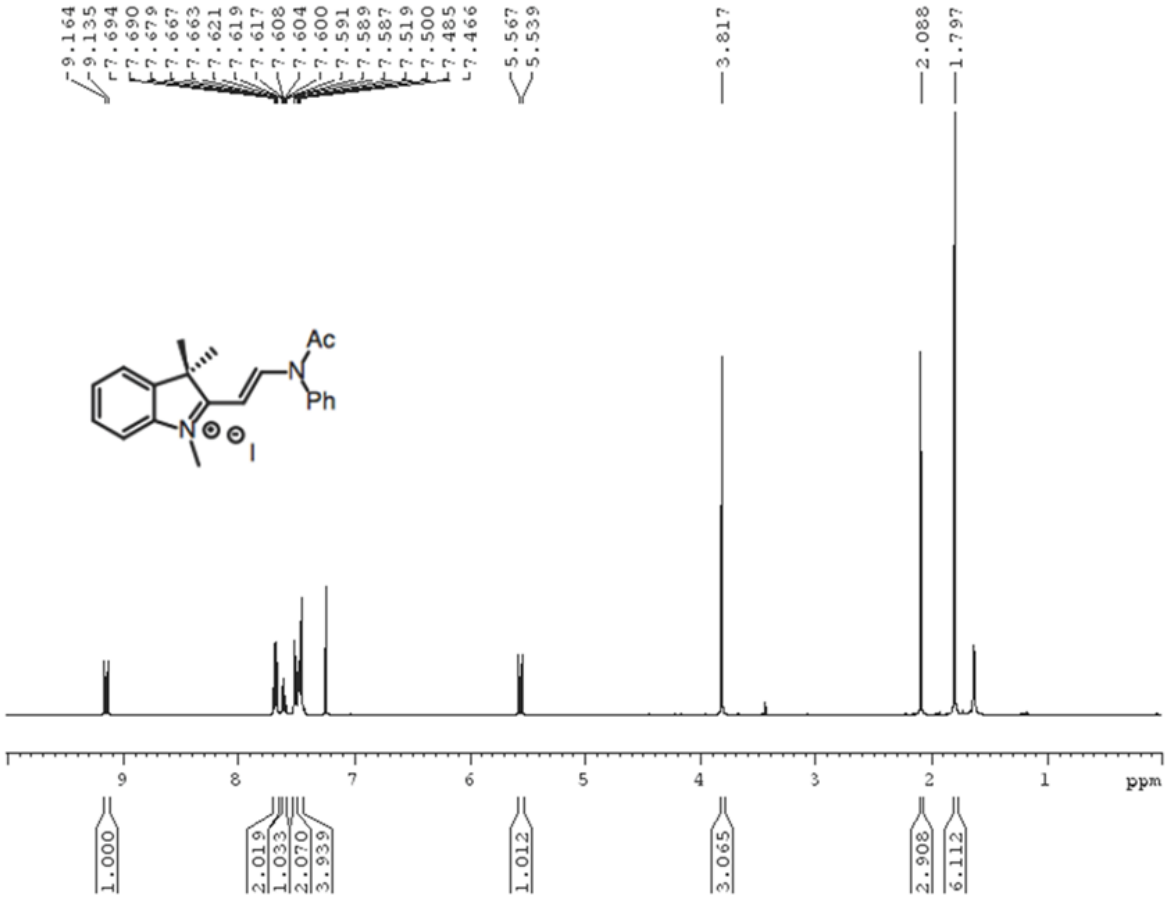

^{1}H NMR spectrum of acetamide-functionalized indolium salt (compound 104). NMR = Nuclear magnetic resonance.

Supplemental figure 21.

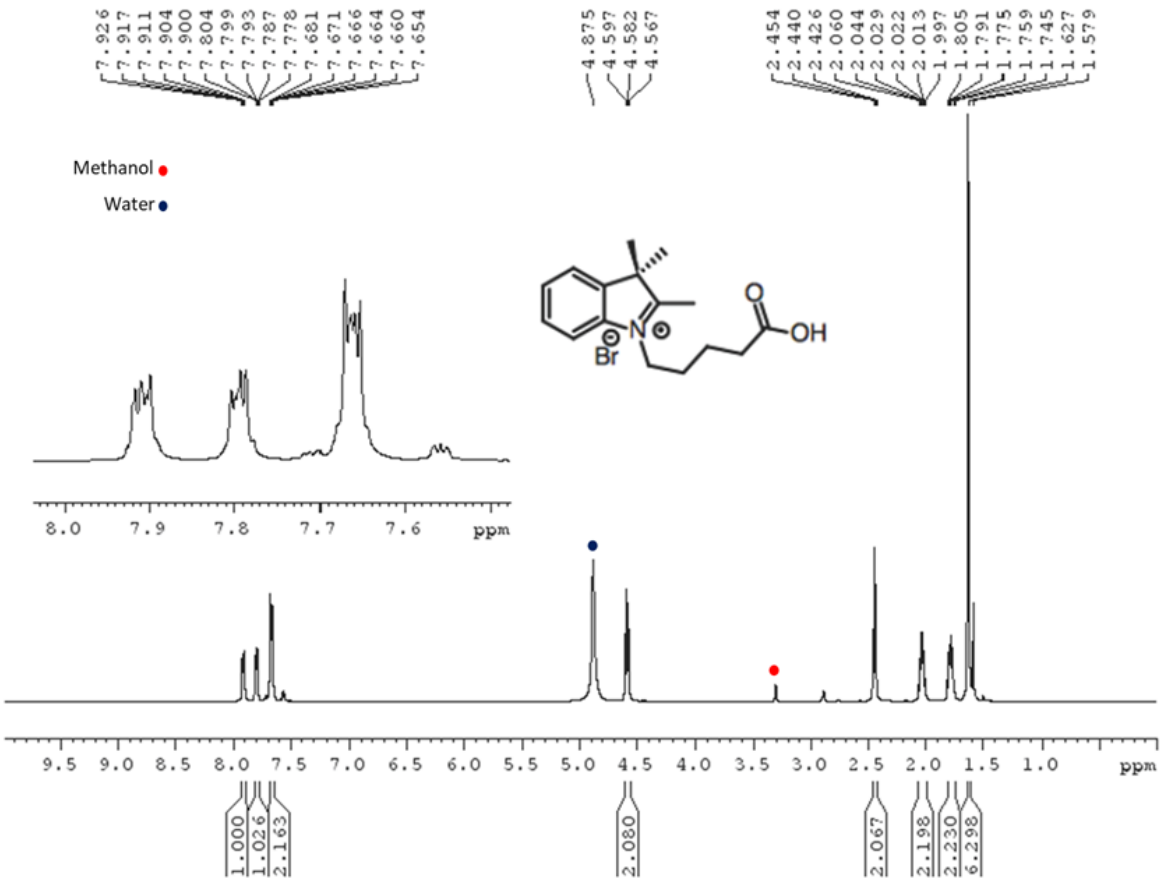

^{1}H NMR spectrum of carboxylate-functionalized indolium salt (compound 105). NMR = Nuclear magnetic resonance.

Supplemental figure 22.

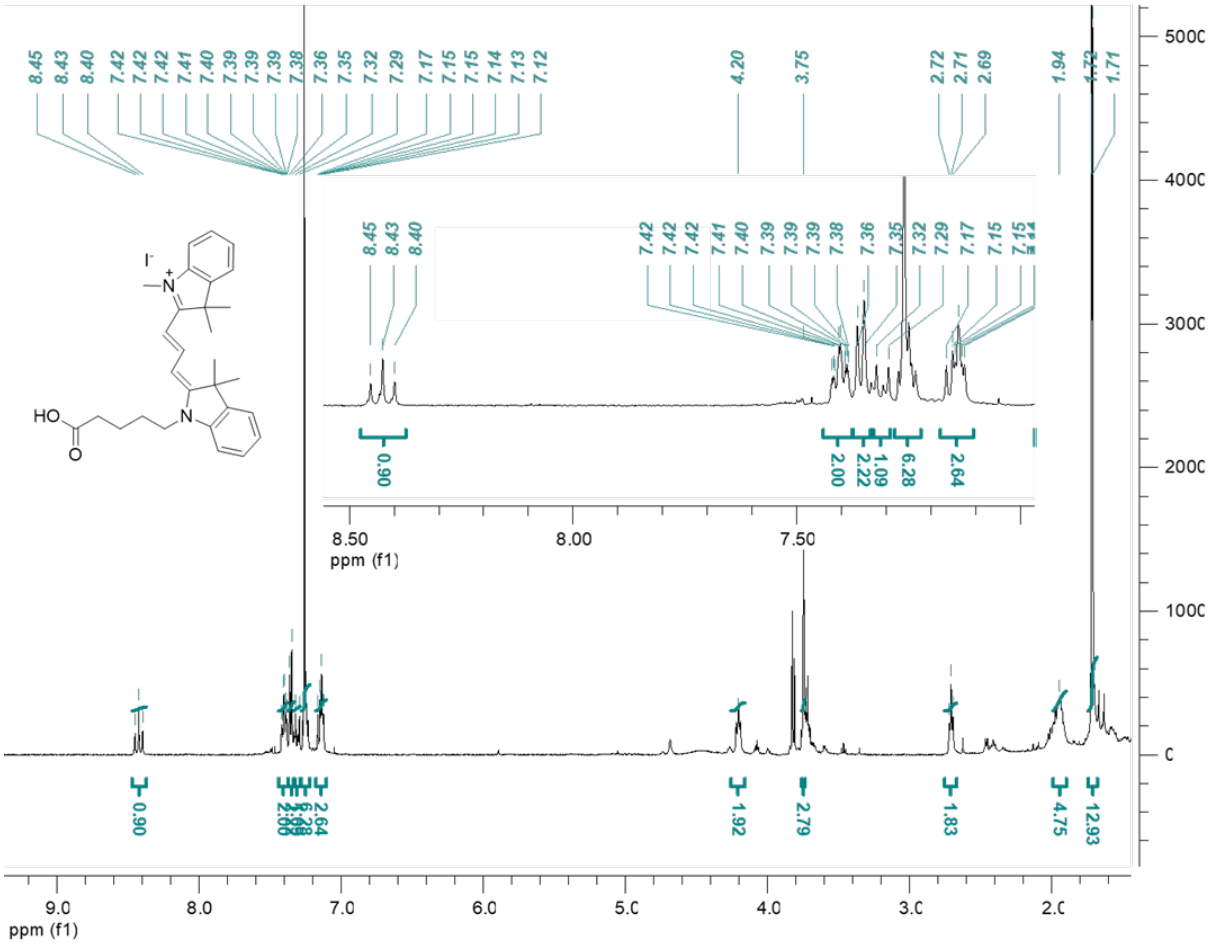

[1]H NMR spectrum of dye Cy3 (compound 106). NMR = Nuclear magnetic resonance.

Supplemental figure 23.

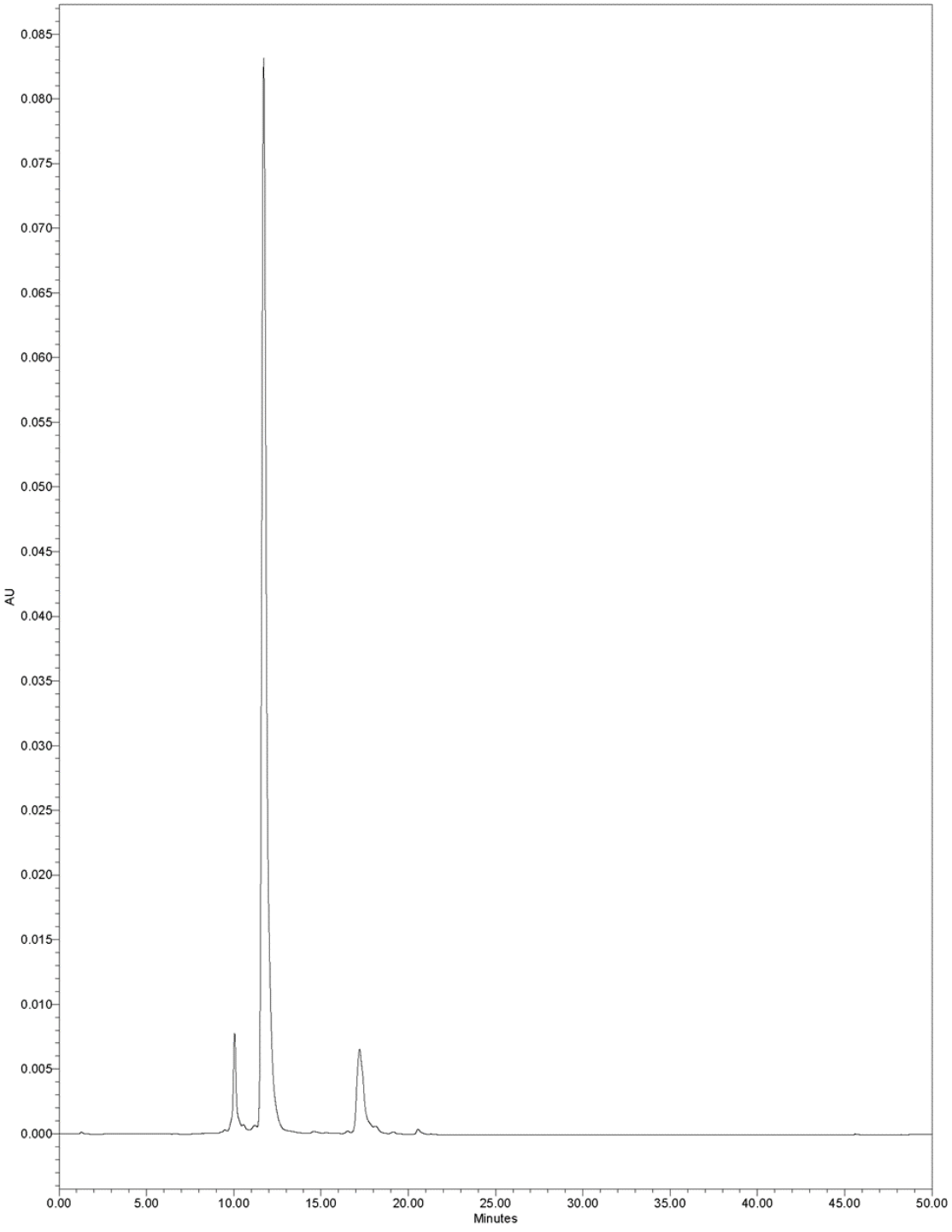

HPLC spectrum of GB2-Cy3 (compound 106) at 546 nm. HPLC = High performance liquid chromatography.

Supplemental figure 24.

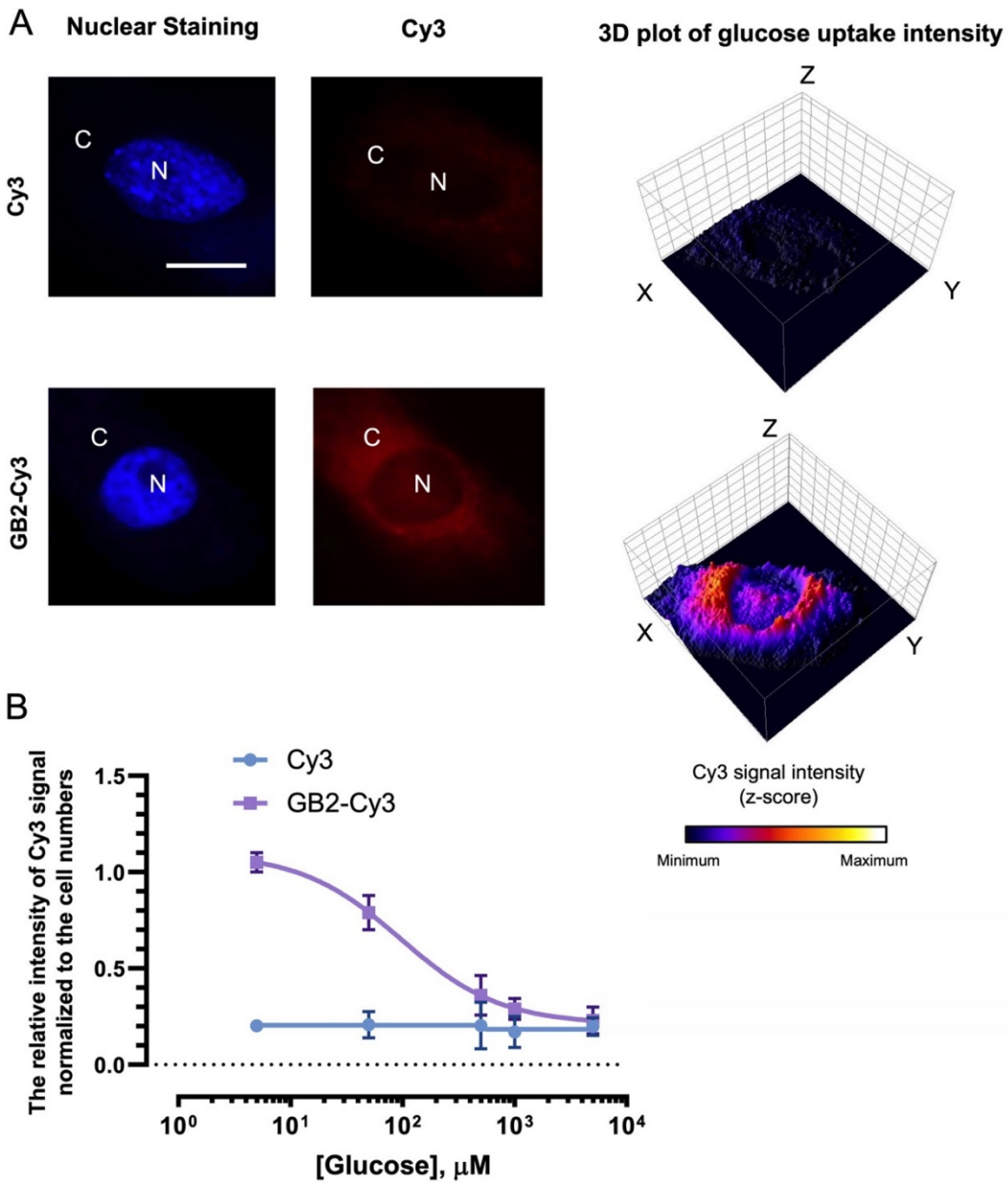

GB2-Cy3 uptake and localization in LNCaP cell line. (A) Free-Cy3 dye showed no specific uptake in LNCaP cells while GB2-Cy3 had high uptake in cytoplasm (showed by C letter) and a minimal intensity in nuclear region (shown by N letter). (B) Glucose competition assay using Cy3 and GB2-Cy3 shows the uptake of GB2-Cy3 by LNCaP cell line could be inhibited as a result of increasing the concentration of glucose.

Supplemental figure 25.

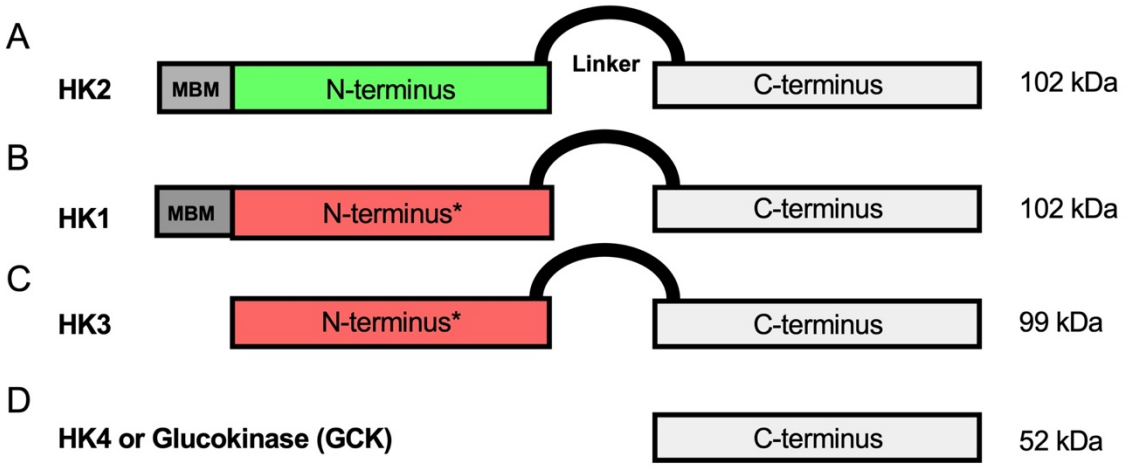

(A-D) Schematic of the structural domains of the isoforms of human HK proteins including HK1, HK2, HK3 and HK4 or glucokinase (GCK). HK1, 2 and 3 are around 100 kDa while glucokinase is about 50 kDa. N-terminus and C-terminus domains have functional catalytic activity in HK2 while N-terminus domains in HK1 and 3 are non-functional. Mitochondrial binding motif (MBF) at the N-terminal domain can be seen only in HK2 and 1. *: non-functional domain. Adopted and modified with permission (*5*).

Supplemental figure 26.

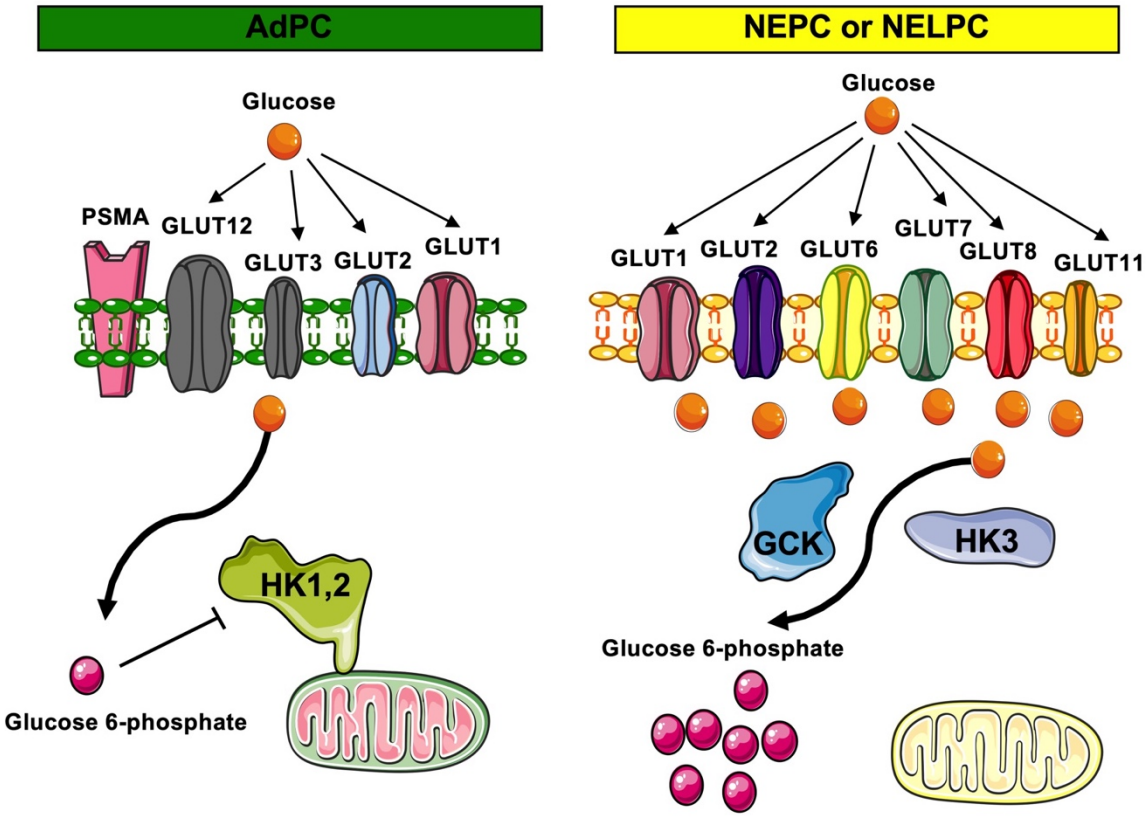

The differential expression of GLUT and HK genes favor higher glucose uptake in NEPC / NELPC in comparison with AdPC. Schematic shows the expression of high affinity GLUT genes found to be elevated in NEPC and NELPC and it could result in increased transport of glucose to the cytoplasm. Drastic elevation of glucose sensor GCK in NEPC and NELPC is also demonstrated in this work. Some elements of this figure were produced using Servier Medical Art image bank (www.servier.com). GCK = Glucokinase

REFERENCE for supplemental figures

1. Beltran H, Prandi D, Mosquera JM, et al. Divergent clonal evolution of castration resistant neuroendocrine prostate cancer. *Nat Med.* 2016;22:298-305.

2. Tsai HK, Lehrer J, Alshalalfa M, Erho N, Davicioni E, Lotan TL. Gene expression signatures of neuroendocrine prostate cancer and primary small cell prostatic carcinoma. *BMC Cancer.* 2017;17:759.

3. Taylor BS, Schultz N, Hieronymus H, et al. Integrative genomic profiling of human prostate cancer. *Cancer Cell.* 2010;18:11-22.

4. Bluemn EG, Coleman IM, Lucas JM, et al. Androgen receptor pathway-independent prostate cancer is sustained through FGF signaling. *Cancer Cell.* 2017;32:474-489.e476.

5. Roberts DJ, Miyamoto S. Hexokinase II integrates energy metabolism and cellular protection: Akting on mitochondria and TORCing to autophagy. *Cell Death Differ.* 2015;22:364.

Supplemental Table 1

An overview of the studied genes in MSKCC cohort *(3)*.

Gene name	Protein name	Assigned cluster	Type of alteration in NELPC	Pearson correlation coefficient with *SRRM4*	Probability of freedom from BCR (*P*-value)	Gleason Score progression (*P*-value)
SLC2A1	GLUT1	*REST*	No alteration	0.0082	0.0026	0.001
SLC2A2	GLUT2	*SRRM4*	↑↑↑	0.69	0.019	0.003
SLC2A3	GLUT3	*REST*	↓↓	0.036	0.0042	0.0024
SLC2A4	GLUT4	*REST*	No alteration	0.0002	0.254	0.22
SLC2A5	GLUT5	*REST*	↓	0.025	0.81	0.56
SLC2A6	GLUT6	*SRRM4*	↑↑↑	0.79	0.039	0.01
SLC2A7	GLUT7	*SRRM4*	↑↑↑	0.8	0.04	0.01
SLC2A8	GLUT8	*SRRM4*	↑↑	0.33	0.357	0.03
SLC2A9	GLUT9	*REST*	↑	0.06	0.892	0.74
SLC2A10	GLUT10	*REST*	↓	0.02	0.182	0.57
SLC2A11	GLUT11	*SRRM4*	↑↑↑	0.63	0.038	0.029
SLC2A12	GLUT12	*REST*	↓↓	0.098	0.012	0.013
SLC2A13	GLUT13 (HMIT)	*REST*	No alteration	0.003	0.816	0.90
SLC2A14	GLUT14	*REST*	↓↓	0.02	0.0056	0.003
HK1	Hexokinase-I	*REST*	↓↓↓	0.26	0.0021	0.00072
HK2	Hexokinase-II	*REST*	No alteration	0018	0.58	0.81
HK3	Hexokinase-III	*SRRM4*	↑↑↑	0.78	0.036	0.019
GCK	Hexokinase-IV (glucokinase)	*SRRM4*	↑↑↑	0.84	0.015	0.00032